Princeton/$\mu\mu$/97-8
C. Lu, K.T. McDonald, E.J. Prebys and S.E. Vahsen
July 24, 1997, revised May. 15, 1998

A Detector Scenario for the Muon Cooling Experiment

1 Introduction

As a verification of the concept of ionization cooling of a muon beam the Muon Collider Collaboration is designing an experiment to cool the 6-dimensional normalized emittance by a factor of two. This note presents a detector to measure the 6-dimensional emittance before and after the cooling apparatus. Figure 1 sketches the layout. See also Fig. 2 in sec. 4.

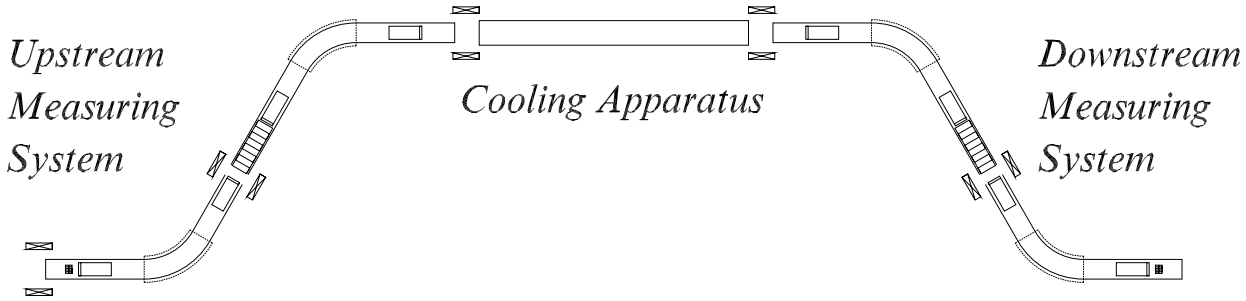

Figure 1: Top view of the layout of the detectors and a 3-T, 30-cm-diameter bent solenoid muon channel surrounding the muon cooling apparatus. Each detector arm is about 8 m long. Vertical guiding dipole fields of 0.55 T are superimposed on the solenoid bends to keep the central trajectory in the horizontal plane.

1.1 Measurement of Individual Muons

To avoid the cost associated with preparation of a muon beam bunched at 800 MHz, the nominal frequency of the RF in the muon cooler, we propose to use an unbunched muon beam. Muons will be measured in the detector individually, and a subset chosen corresponding to an ideal input bunch. The muons are remeasured after the cooling apparatus and the output bunch emittance calculated to show the expected reduction in phase-space volume. The technique of tracing individual muons will reproduce all effects encountered by a bunch except for space-charge.

1.2 The Critical Role of the Timing Measurement

Five of the six phase-space parameters, the transverse coordinates x, x', y, y' and the momentum P, are typically measured in detectors of elementary particles to an appropriate accuracy. The sixth parameter, z, or equivalently, time t relative to the bunch center must be known to a small fraction of a cycle of the 800-MHz RF, *i.e.*, to a few picoseconds.

The time must be measured to this accuracy or muons cannot be selected as representative of the muon bunch we desire to study. This demanding requirement has a strong influence on the choice of detection techniques. At present we believe the best option is the use of an RF accelerating cavity phased to impart zero energy to a particle in time with the center of the bunch. Such a cavity imparts a correlation between energy (and hence momentum) and time within the bunch. Then measurement of the muon's momentum before and after the RF cavity permits inference of the desired time. A cost of this technique is the fourfold momentum measurement of each muon: twice before the cooling apparatus and twice after.

For the RF timing measurement to function, we must know the muon's time to about 1/4 cycle = 300 ps via an auxiliary measurement.

While the resolution of the momentum spectrometer at the nominal beam momentum of 165 MeV/c is degraded by multiple scattering in even fairly small amounts of material, the process of correlating time with momentum in the RF cavity is very insensitive to the amount of material in the cavity.

1.3 Confinement of the Muon Beam in a Bent Solenoid Channel

Another striking feature of the experiment is the relatively large transverse emittance of the idealized bunch under study. It is believed that the only way to contain the beam over the lengthy transport is for it to be within a several-Tesla magnetic field parallel to the beam direction. The logical consequence is that all detector elements must function within this high field. Further, the dispersion required for the momentum measurement should be provided by confining field. Here we consider the use of a bent solenoid channel, shown in Figs. 1 and 2, rather than the hybrid system of ordinary solenoids and (transverse) dipoles studied by Rick Fernow. Two bent solenoids are linked by ordinary solenoids to form the muon channel of the upstream arm of the detector; another two bent solenoids from the downstream arm.

Supposing the bend plane of the bent solenoids (more properly called toroidal sectors) is horizontal, the beam experiences a net vertical displacement (called 'curvature drift' in the plasma-physics community) of tens of cm while traversing the bend. This displacement is cancelled for muons at the central momentum by 'guiding dipole' magnets whose vertical 0.55-T field is superimposed on the bend region of the solenoid channel. Off-momentum muons are dispersed vertically – although the bend of the solenoid channel is horizontal.

The limiting aperture of the solenoid channel is the effective maximum radius of the RF timing cavity. For a cylindrical $TM_{0,1,0}$ cavity the acceleration is still one half maximum at 2/3 of the cavity radius, which we taking to be the maximum useful radius. For an 800-MHz cavity, the usable radius is then 10 cm; for a 400-MHz cavity it would be 20 cm.

Analytic calculations and numerical simulation indicate that a beam of 165-MeV/c muons of normalized transverse emittance $\epsilon_x = 1500\pi$ mm-mrad that has been prepared with a $\beta^\star$

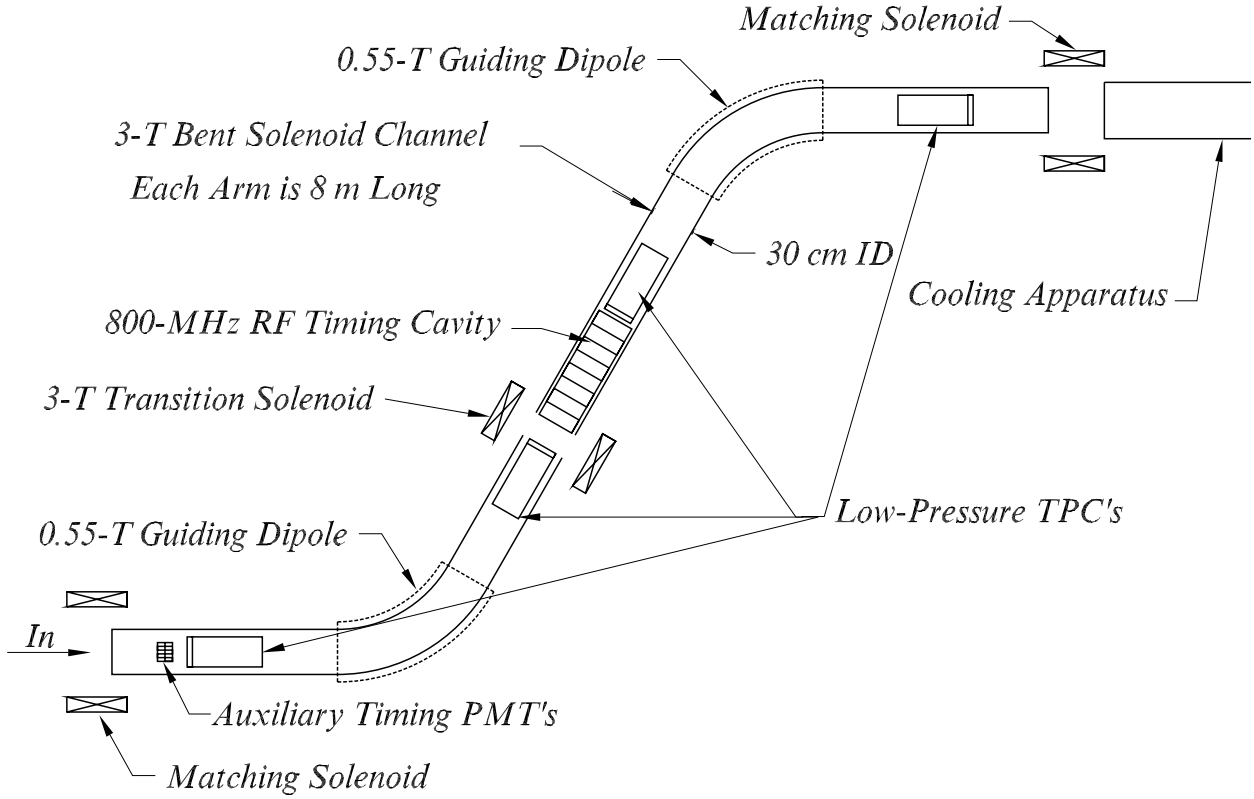

Figure 2: Layout of the "before" arm of the detector.

of 37.7 cm can be contained with rms transverse width of $\sigma_R = 3$ cm by a 3-T solenoid field (or within $\sigma_R = 5.6$ cm in a 1.5-T field). The detectors would cover out to a radius of 10 cm, or $3.3\sigma_R$. To allow for detector infrastructure inside the solenoids but outside the fiducial volume, the inner radius of the solenoid channel will be 15 cm (or 24 cm if the RF frequency is 400 MHz)

A cost estimate based on a scaling law derived from numerous existing superconducting solenoids indicates that each of the four 4-m-long bent solenoid sections would cost about \$710k for a 3-T field and 30-cm inner radius (or \$530k for a 1.5-T field and 48-cm inner diameter). To keep the cost down the detector-solenoid channel operates at lower field than that in the FOFO cooling apparatus, and consequently with a larger $\beta^\star$. Matching solenoids will be required at both the entrance and exit of each detector arm.

The power feed for the RF timing cavity requires a break in the solenoid channel midway in each 8-meter arm. To keep the field uniform in the beam region a large radius, 3-T transition solenoid will surround the gap where the RF power enters.

1.4 Low-Pressure Time-Projection Chambers

The principal detectors are position-measuring devices. Angles are reconstructed by comparing the muon's position at various distances along the beam axis. The muon momentum is measured by comparing angles on either side of the bent solenoids. As the muons have

relatively low momentum, multiple scattering in detector material, and even in atmospheric-pressure gas is significant. Hence we propose that each arm of the detector be a low-pressure device with minimal internal structure.

The muons will be detected by the ionization of 8.4-Torr methane (if the temperature is 20°C) corresponding to one ion pair per 3 cm of track length. Methane is still a gas a liquid-nitrogen temperature for pressures below 10 Torr. Hence the tracking chambers, which are inside the bore of the superconducting solenoids, could be operated near 77°K resulting in a lower thermal load on the magnet cryogenic system. At 77°K a gas pressure of 2.2 Torr leads to the same density (and hence ionization density) as does 8.4 Torr at 20°C.

The tracking chamber must reconstruct the center of curvature of the helical orbit of the muons in the solenoid field. In the strong magnetic field of the detector the ionization electrons drift easily only along the field lines. Hence the collection electric field should be aligned with the magnetic field. This leads to a detector geometry popularly known as a time-projection chamber (TPC).

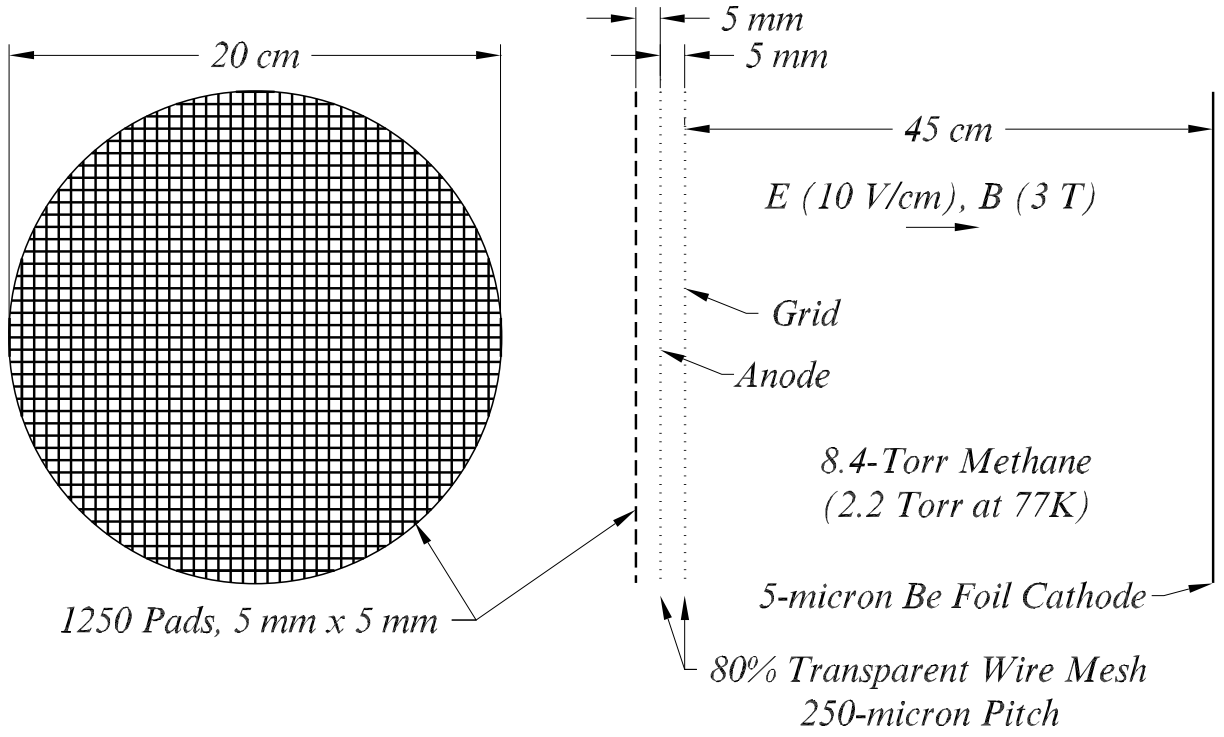

Figure 3: Sketch of the low-pressure time projection chamber.

The drift velocity of ionization electrons is a function of E/P, where here E is the electric field and P is the gas pressure. Hence the saturation drift velocity of 100 μm/ns (methane) is achieved at a field of only 10 V/cm at 8.4-Torr pressure. The proposed TPC is not a high-voltage device.

Gas gain is obtained near a wire mesh anode plane in a gap separated from the ionization/drift region by a wire-mesh grid, as shown in Fig. 3. The induced pulse on a 10-cm-radius cathode plane subdivided into 1250 5×5 mm^2 pads yields x and y coordinates to 200 μm

via charge interpolation. Each pad is sampled at 50 MHz, which samples are stored in a 512-deep switched-capacitor array and multiplexed into a 12-bit ADC between beam pulses. Interpolation of the samples in time will locate the z coordinate to 200 μm. Over a total drift distance of 45 cm, the TPC will observe 15 points on a track segment, and measure its angle to accuracy of about 1 mrad. The momentum resolution, σ_P/P, of each spectrometer consisting of a bent solenoid surrounded by a pair of TPC's will be 0.0014 at 165 MeV/c.

The total drift time of the ionization electrons is about 4.5 μsec, which is of the same order as, perhaps even longer than, the active time of the RF system of the cooling apparatus. So in effect, the detector concurrently samples all muons in a single RF macropulse. To successfully isolate each of these muons there should be no more than about 10 muons per macropulse, independent of its length so long as it is in the range of 50 ns-4.5 μs.

A higher rate capability could only be achieved with a detector with shorter drift times, and hence more walls and higher channel count. The additional walls will compromise the angular resolution due to multiple scattering, while the higher channel count raises the detector cost.

To achieve good spatial resolution over their 45-cm length, the low-pressure TPC's should be located in regions where the magnetic field is well understood and as uniform as possible. Hence the TPC's should be located at least one solenoid diameter back from the ends of the straight sections.

The 2-m-long region between TPC's in each momentum spectrometer could be filled with helium, at the same pressure as the TPC gas, to minimize multiple scattering. The TPC electrodes facing the bent solenoids will be made of 5-μm-thick beryllium, which could also form the gas boundary between methane in the TPC and helium in the bent solenoid.

1.5 Auxiliary Timing Measurement

As mentioned above, we must know the muon's time to about 300 ps for proper interpretation of the RF timing measurement. Also, it will be extremely helpful to have a timing measurement of each muon to accuracy of 1 ns to mark the start of the drift time in the TPC detectors.

A 100-ps timing measurement could be accomplished in a 1.5-T field region with scintillation counters and fine-mesh photomultipliers. In a 3-T field we may have to use microchannel-plate PMT's. The auxiliary timing measurement can be combined with the RF timing measurement to identify electrons, muons and pions by time of flight.

1.6 Cost

- The bent solenoid channel, including guiding dipoles and matching solenoids, is estimated to cost about \$4M.
- The two RF timing cavities operate at the same frequency as the cooling apparatus, and will add about \$0.5-1M to the RF budget.
- The 8 TPC detectors have a total channel count of about 10,000. Their cost will be dominated by that of the readout, which at about \$100/channel totals \$1M.

- An auxiliary timing detector based on fine-mesh photomultipliers would cost about \$0.2M, but would cost close to \$1M if MCP-PMT's must be used.
- Thus the total detector cost is in the range \$5.7-6.5M.

1.7 Near-Term R&D

The low-pressure tracking chamber is not novel in principle, but it would be well to build a prototype of proposed configuration during the next 18 months. The scale of the required effort in about \$100k in equipment.

The auxiliary timing device is relatively standard if based on fine-mesh photomultipliers and scintillator bars. A prototype of two bars each with two PMT's could be built for \$30k, or \$50k for MCP-PMT's.

The RF timing cavity is presumed to be of similar design to those of the FOFO cooling channel. Prototypes of the FOFO RF cavities could well serve as the final timing cavities, and so little independent R&D is needed here.

The bent solenoid sections are somewhat novel. Each is estimated to cost about \$700k. Construction of one section as an R&D project would be the costliest item in the proposed R&D budget.

2 Detector Requirements

2.1 Combined Accuracy

Ignoring correlations, the 6-dimensional emittance ϵ of the muon beam is the product of the rms widths of the projections of the muon population on the six phase-space axes x, P_x, y, P_y, z and P_z. We take the z-axis as parallel to the beam. We generally consider the trace space with axes x, x', y, y', $z = \beta_z ct$ and $P_z \approx P$ rather than the formal phase space. However, we use the term 'phase space' for either the trace space or the canonical phase space.

We label a variance (second moment) of the distribution of muons by σ_i^2 where i indicates one of the six phase-space axes. We call σ_i the rms width. The uncertainty in σ_i is labelled δ_{σ_i}. Then the emittance is

$$\epsilon = \prod_{i=1}^{6} \sigma_i, \tag{1}$$

and the corresponding uncertainty is

$$\frac{\delta_\epsilon}{\epsilon} = \sqrt{\sum_{i=1}^{6} \left(\frac{\delta_{\sigma_i}}{\sigma_i}\right)^2}. \tag{2}$$

Supposing the relative uncertainty is the same in all six projections, we have

$$\frac{\delta_\epsilon}{\epsilon} = \sqrt{6}\frac{\delta_\sigma}{\sigma}. \tag{3}$$

In the cooling experiment it is proposed to demonstrate a factor of two reduction in the 6-D emittance. Before this large a reduction is observed we will likely pass through stages with smaller reduction. Hence the measurement uncertainty, δ_ϵ/ϵ, should be much less than 1/2; a goal of 3% uncertainty has been set. Then eq. (3) implies that the relative uncertainty in the rms width of the projection of phase space onto each of the six axes should be only 1%.

2.2 Effect of Detector Resolution

For several phase-space axes the ratio of the rms width σ_D of the detector resolution function to the rms width σ_i of the projected distribution is larger than 1%; *i.e.*, $\sigma_D/\sigma_i > 0.01$. Typically, multiple scattering is the cause of poor detector resolution. Can we achieve the desired measurement accuracy of $\delta_{\sigma_i}/\sigma_i$ in this case?

In the Gaussian approximation, the observed rms width σ_O of the projected phase-space distribution is sum in quadrature of the 'true' rms width σ_i and the rms width σ_D of the detector resolution:

$$\sigma_O^2 = \sigma_i^2 + \sigma_D^2. \tag{4}$$

We suppose that σ_D is known to an accuracy δ_{σ_D}. Then, we extract the desired rms width σ_i according to

$$\sigma_i^2 = \sigma_O^2 - \sigma_D^2. \tag{5}$$

We now wish to characterize the uncertainty δ_{σ_i}. From eq. (5) we find

$$\delta_{\sigma_i^2}^2 = \delta_{\sigma_O^2}^2 + \delta_{\sigma_D^2}^2. \tag{6}$$

Next, the uncertainty in the observed variance σ_O^2 after a set of N measurements is[1]

$$\delta_{\sigma_O^2} = \sqrt{\frac{2}{N}}\sigma_O^2 = \sqrt{\frac{2}{N}}\left(\sigma_i^2 + \sigma_D^2\right). \tag{7}$$

Then, noting that $\delta_{\sigma^2} = 2\sigma\delta_\sigma$ we find the key result:

$$\left(\frac{\delta_{\sigma_i}}{\sigma_i}\right)^2 = \frac{1}{2N}\left(1 + \frac{\sigma_D^2}{\sigma_i^2}\right)^2 + \left(\frac{\sigma_D}{\sigma_i}\right)^4\left(\frac{\delta_{\sigma_D}}{\sigma_D}\right)^2. \tag{8}$$

2.2.1 Perfectly Known Resolution

In the limit that the detector resolution is completely understood we have $\delta_{\sigma_D} = 0$, and the relative uncertainty in the rms width σ_i is

$$\frac{\delta_{\sigma_i}}{\sigma_i} = \sqrt{\frac{1}{2N}}\left(1 + \frac{\sigma_D^2}{\sigma_i^2}\right). \tag{9}$$

If the detector resolution σ_D is larger than the rms width σ_i we wish to measure, the number of events required to achieve a specified accuracy, $\delta_{\sigma_i}/\sigma_i$ varies as the fourth power of the ratio σ_D/σ_i.

[1]See, for example, sec. 28.2 of the chapter on *Statistics* of the *Review of Particle Properties* (1996).

Thus, there is a severe statistical penalty unless

$$\sigma_D < \sigma_i. \tag{10}$$

However, once relation (10) is satisfied,

$$\frac{\delta_{\sigma_i}}{\sigma_i} \approx \sqrt{\frac{1}{2N}}. \tag{11}$$

In this case, about 10,000 measurements would be required to reach a 1% relative uncertainty in σ_i

If, say, only 1% of the beam muons occupy the relevant part of phase space, a typical run would require measurement of 10^6 muons.

2.2.2 Large-N Limit

In the other limit that counting statistics, but not detector resolution, can be neglected, we have

$$\frac{\delta_{\sigma_i}}{\sigma_i} = \left(\frac{\sigma_D}{\sigma_i}\right)^2 \frac{\delta_{\sigma_D}}{\sigma_D}. \tag{12}$$

Good results can only be obtained if σ_D/σ_i is less than one, unless the detector resolution is extraordinarly well understood. However, if σ_D/σ_i is much less than one, very good results are possible.

2.2.3 Maximum Acceptable Detector Resolution

To achieve the goal of measurement accuracy $\delta_{\sigma_i}/\sigma_i = 0.01$, we require that the effect of detector resolution be no more than half in quadrature, *i.e.*, $\delta_{\sigma_i}/\sigma_i < 0.007$ as the number of measurements grows large.

We also suppose that the uncertainty in the detector resolution function will be no more than 20%:

$$\frac{\delta_{\sigma_D}}{\sigma_D} < 0.2. \tag{13}$$

Then eq. (12) tells us that the detector resolution must obey

$$\sigma_D < \sqrt{\frac{\delta_{\sigma_i}/\sigma_i}{\delta_{\sigma_D}/\sigma_D}}\sigma_i = 0.19\sigma_i. \tag{14}$$

The first part of expression (14) indicates that if we know the detector resolution function to the same accuracy as we desire for $\delta_{\sigma_i}/\sigma_i$ then the detector resolution can be the same as σ_i. In particular,

$$\text{If} \quad \frac{\delta_{\sigma_D}}{\sigma_D} < 0.01, \quad \text{then we can have} \quad \sigma_D \approx \sigma_i \quad \text{and} \quad \frac{\delta_{\sigma_i}}{\sigma_i} = 0.01. \tag{15}$$

2.3 Phase-Space Parameters

We now consider the specific implications of the previous analysis to measurements of the various phase-space projections. Table 1 lists various parameters of the phase space to be explored in the cooling experiment.

The normalized transverse input emittance we wish to study is $\epsilon_{N,x} = \epsilon_{N,y} \approx 1250\pi$ mm-mrad for a nominal beam momentum of 165 MeV/c. Then, $\gamma = 1.85,\ \beta = 0.84$, and the geometric transverse emittance is $\epsilon_x = \epsilon_y = \epsilon_N/\gamma\beta = 800$ mm-mrad. The cooling apparatus is expected to operate with input $\beta^\star \approx 10$ cm, so the characteristic width of the transverse phase-space distributions are $\sigma_x = \sigma_y \approx 9$ mm, and $\sigma_{x'} = \sigma_{y'} \approx 90$ mrad. The output $\beta^\star$ is expected to be about 10 cm also.

Of course, the $\beta^\star$ in the muon channel of the detector need not be the same as that in the cooling apparatus. Matching solenoid magnets would, however, be required if (as argued below) the detector $\beta^\star$ is larger than 10 cm.

Table 1: Phase-space parameters of the FOFO-channel cooling experiment.

Parameter	Input Value	Output Value
P (MeV/c)	165	165
E (MeV)	198	198
γ	1.85	1.85
β	0.84	0.84
$\gamma\beta$	1.56	1.56
$\epsilon_{x,N} = \epsilon_{y,N}$ (π mm-mrad)	1250	625
$\epsilon_x = \epsilon_y$ (π mm-mrad)	800	400
$\beta^\star$ (cm)	10	10
$\sigma_x = \sigma_y$ (mm)	9	9
$\sigma_{x'} = \sigma_{y'}$ (mrad)	90	63
σ_P/P	0.03	0.04
$\sigma_E/E = \beta^2\sigma_P/P$	0.021	0.028
σ_z (cm)	1	1.2
$\sigma_t = \sigma_z/\beta c$ (ps)	40	48

2.4 Accuracy of Extrapolation of the Emittance Along the Beam

The transverse emittance is measured separately in each of the 8 TPC's. Likewise, the momentum will be known at the position of each of the TPC's. The timing will be directly measured, in effect, at the center of the RF timing cavity. However, for the cooling experiment we need to know the 6-D emittance at the entrance and exit of the cooling apparatus. This requires extrapolation of the timing over about 4 meters. Combining eq. (14) with the values in Table 1, we can achieve accuracy $\delta_{\sigma_t} = 0.4$ ps if the time resolution $\sigma_{t,D}$ of

the detector after extrapolation by 4 m is 8 ps; and we must know this resolution to an uncertainty of 1.5 ps. We could relax the requirement on time resolution to, say, $\sigma_{t,D} = 16$ ps only if the uncertainty in the time resolution is reduced to 0.6 ps.

When we extrapolate over a distance L along the beam the resulting uncertainty in the corresponding time step, $t = L/\beta_z c = L/\beta c \cos\theta$, due to uncertainty in momentum is

$$\delta t = \frac{L}{\beta^2 c \cos\theta}\delta\beta = \frac{L}{\gamma^2\beta_z c}\frac{\delta P}{P} \approx 1000 \text{ [ps]} \left[\frac{L}{1 \text{ m}}\right]\frac{\delta P}{P}, \tag{16}$$

where θ is the angle of the trajectory to the z-axis. Hence, the desired uncertainty on the time extrapolation that $\delta_t < 8$ ps after 4 m sets a requirement on momentum resolution that $\sigma_{P,D}/P < 0.002$.

Similarly the sensitivity of the time extrapolation to the uncertainty in angle θ is

$$\delta t = \frac{L\tan\theta}{\beta_z c}\delta\theta \approx 4000 \text{ [ps]} \left[\frac{L}{1 \text{ m}}\right]\tan\theta\delta\theta. \tag{17}$$

Hence, the desired uncertainty on the time extrapolation that $\delta_t < 8$ ps after 4 m sets a requirement on angular resolution that $\sigma_{\theta,D} < 0.0005/\tan\theta$. We will find later that in the detector the $\beta^\star$ should be increased to about 1 m, corresponding to rms θ of 0.03. Then the timing extrapolation is accurate enough so long as $\sigma_{\theta,D} < 0.017$, which is not very demanding.

Of course, muons with momentum and angles at, say, $3\sigma_{P,D}$ and $3\sigma_{\theta,D}$ will suffer larger extrapolation errors, so we prefer to exceed the requirements just stated if possible. Also, the two uncertainties (16) and (17) add in quadrature to the measurement uncertainty $\sigma_{t,D,\text{cavity}}$ at the rf cavity to determine the total uncertainty in the extrapolated time. To account for these effects we specify requirements $\sqrt{2}$ tighter:

$$\frac{\sigma_{P,D}}{P} < 0.0014, \quad \sigma_{\theta,D} < 0.011 \quad \text{(Time extrapolation)}, \quad \text{and} \quad \sigma_{t,D,\text{cavity}} = 6 \text{ ps}. \tag{18}$$

The time extrapolation requires better momentum resolution than does the direct measurement of either momentum (need only $\sigma_{P,D}/P = 0.006$) or time (see sec. 3.3).

2.5 Accuracy of Momentum Measurement

Use of a bent solenoid inside a guiding dipole in a momentum spectrometer leads to some features that may be unfamiliar. In particular, the momentum dispersion is vertical when the overall bend is horizontal.

2.5.1 Larmor Frequency, Period, and Radius

The trajectory of a muon in a straight solenoid with magnetic field $\mathbf{B}_s$ is a helix, whose axis we will call the 'guiding ray'. The projection of the trajectory onto a plane perpendicular to the guiding ray is a circle of radius R_{curv}. In this plane the equation of motion is (in MKSA units)

$$\frac{\gamma m v_\perp^2}{R_{\text{curv}}} = \gamma m \Omega_B v_\perp = e v_\perp B_s, \tag{19}$$

so the Larmor frequency Ω_B is

$$\Omega_B = \frac{v_\perp}{R_{\rm curv}} = \frac{\beta c \sin\theta}{R_{\rm curv}} = \frac{ec^2 B_s}{\gamma mc^2} = \frac{(3\times10^8)^2}{105.6\times10^6}\frac{B_s\ [\rm T]}{\gamma} = 0.852\ \rm GHz\frac{B_s\ [T]}{\gamma}, \tag{20}$$

where as before θ is the angle between the muon trajectory and the guiding ray. During one Larmor period the muon advances distance λ_B given by

$$\lambda_B\ [\rm m] = \frac{2\pi\beta_z c}{\Omega_B} = \frac{2\pi P_z}{eB_s} \approx \frac{2\pi P}{eB_s} = \frac{2\pi\times10^6}{3\times10^8}\frac{P\ [\rm MeV/\mathit{c}]}{B_s\ [\rm T]} = 2\pi\frac{P\ [\rm MeV/\mathit{c}]}{300 B_s\ [\rm T]}. \tag{21}$$

The radius of curvature of the helical trajectory follows from (20):

$$R_{\rm curv}\ [\rm m] = \frac{P_\perp}{eB_s} = \frac{P}{eB_s}\sin\theta = \frac{P\ [\rm MeV/\mathit{c}]}{300 B_s\ [\rm T]}\sin\theta. \tag{22}$$

For example, 165-MeV/c muons in a 3-T field have Larmor frequency $\Omega_B = 1389$ MHz and period $\lambda_B = 1.15$ m. The helix radius of curvature is $R_{\rm curv} = 18.3\sin\theta$ cm.

2.5.2 Curvature Drift

A bent solenoid is actually a sector of a toroidal field, so ideally the magnetic field varies as $1/R_{\rm curv}$ in the bend plane, and does not vary transversely to the bend plane. A muon moving in the field of the bent solenoid spirals around a 'guiding ray' that follows a magnetic field line in the zeroeth approximation. However, in a better approximation the 'guiding ray' is deflected out of the bend plane by effects sometimes called the 'curvature drift' and the 'grad-**B** drift' in the plasma-physics community [2]. Briefly, the muon encounters a transverse, horizontal component of the magnetic field as it moves around the bend, so the corresponding $\mathbf{v}\times\mathbf{B}$ force is perpendicular to the bend plane.

First consider the case of no vertical guiding magnetic field. Lines of the bent solenoid field $\mathbf{B}_s$ are assumed to be horizontal circles. The guiding ray of a muon is in a horizontal circle of radius $R_{\rm bend}$ to the first approximation.

We analyze the motion in the frame in which the forward motion of the muon is zero. This is a rotating frame with laboratory angular velocity $\Omega = \beta_z c/R_{\rm bend} \approx \beta c/R_{\rm bend}$. Then in the rotating frame the muon experiences a centrifugal force horizontally outwards of magnitude

$$F_{\rm cent} = \gamma m\Omega^2 R_{\rm bend} \approx \frac{\gamma mc^2\beta^2}{R_{\rm bend}}. \tag{23}$$

This fictitious force can be conveniently thought of as arising from a fictitious electric field

$$E_{\rm cent} \approx \frac{\gamma mc^2\beta^2}{eR_{\rm bend}} \tag{24}$$

pointed horizontally outwards.

The motion of the muon in the rotating frame then results from the crossed fields $\mathbf{E}_{\rm cent}$ and $\mathbf{B}_s$. As is well known, the motion consists of an oscillatory part and a drift. The oscillatory part is at the Larmor frequency discussed above. Here we wish to isolate the

drift velocity, which we do be requiring the Lorentz force associated with $\mathbf{v}_{\rm drift}$ to cancel the centrifugal force:

$$0 = e[\mathbf{E}_{\rm cent} + \mathbf{v}_{\rm drift} \times \mathbf{B}_s], \tag{25}$$

and hence

$$v_{\rm drift} = \frac{E_{\rm cent}}{B_s} \approx \frac{\gamma mc^2\beta^2}{eR_{\rm bend}B_s} = \frac{P}{eB_s}\frac{\beta c}{R_{\rm bend}}. \tag{26}$$

This is the curvature drift, which is vertical in case of a solenoid bent in the horizontal plane. Since a vertical motion is observed to be the same in both the rotating frame and the laboratory frame, our analysis holds in the latter frame as well. The drift velocity is proportional to momentum, and inversely proportional to the solenoid field strength. Thus the bent solenoid disperses the muon beam vertically.

Because the bent solenoid is really a toroid the field strength varies as $1/R_{\rm curv}$. This variation leads to a small correction to eq. (26) due to the 'grad-**B** force', which we neglect in the present discussion.

For 165-MeV/c muons in a 3-T bent solenoid with a 1-m bend radius the vertical drift velocity would displace the beam by about 16 cm vertically per meter of path. By itself, a bent solenoid leads to a troublesome nonplanar trajectory for the central ray.

2.5.3 Bent Solenoid with a Guiding Dipole

The curvature drift (26) can be cancelled for a specific momentum if a vertical magnetic field is superimposed on the horizontal bent solenoid. The vertical field strength is chosen such that the radius of curvature of the trajectory of a muon of momentum P_0 is exactly the bend radius $R_{\rm bend}$ of the bent solenoid. Then as the 'central' muon (for which $P = P_0$ and $\theta = 0$) moves through the bent solenoid it never encounters a component of the solenoid field perpendicular to its trajectory, and hence is not deflected vertically. This configuration is much more practical for a momentum spectrometer.

The vertical 'guide field' is provided by a 'guiding dipole' that surrounds the bent solenoid. The desired vertical-guide-field strength B_G is thus

$$B_G\ [\rm T] = \frac{P_0}{eR_{\rm bend}} = \frac{P_0\ [\rm MeV/\mathit{c}]}{300R_{\rm bend}\ [\rm m]}, \tag{27}$$

recalling eq. (22). For example, with $P_0 = 165$ MeV/c and $R_{\rm bend} = 1$ m we need a guide field of $B_G = 0.55$ T.

The guide field should cancel the curvature drift for muons of momentum P_0 no matter how far they are from the center of curvature of the bent solenoid. Therefore, the guide field should vary inversely with the distance from the center of curvature, just as does the bent solenoid field. This property is implicit in eq. (27). We find in sec. 2.6.3 that the if the guide field were uniform it would lead to undesirable vertical broadening of the beam.

Muons with momenta different from the central momentum still experience a vertical deflection. To the first approximation the effect of the vertical guide field can be thought of as reducing the curvature drift velocity (26) by the drift velocity of the central ray. Then for a muon with momentum difference ΔP from the central momentum the residual vertical

drift velocity is

$$\Delta v_{\rm drift} \approx \frac{\Delta P}{eB_s}\frac{\beta c}{R_{\rm bend}}. \tag{28}$$

If the bent solenoid has total bend angle $\theta_{\rm bend}$ then the time to cross the bent solenoid is $t = R_{\rm bend}\theta_{\rm bend}/\beta_z c \approx R_{\rm bend}\theta_{\rm bend}/\beta c$, and the resulting vertical deflection is

$$y_G = \Delta v_{\rm drift} t \approx \frac{P_0}{eB_s}\frac{\Delta P}{P_0}\theta_{\rm bend}. \tag{29}$$

It is important to note that eq. (29) describes the deflection of the guiding ray of the muon trajectory and not the trajectory itself. (The exception is a trajectory with $\theta = 0$ at the entrance to the bent solenoid, in which case the guiding ray and the trajectory are identical.) The muon's momentum cannot be determined simply by measuring the height of its trajectory at the entrance and exit of a bent solenoid. Rather, the height of the guiding ray must be reconstructed at both places. Each such reconstruction requires observation of enough of the helical trajectory that its center can be determined.

A counterintuitive aspect of eq. (29) is that the vertical dispersion varies inversely with the strength B_s of the bent solenoid (and does not depend directly on the strength B_G of the guiding dipole). In the next section we show that the accuracy with which the height of the guiding ray can be measured varies as $1/B_s^2$, which restores the expected result that the momentum resolution improves with $1/B_s$.

2.5.4 Momentum Analyzing Power

To use the dispersion, (29), of a bent solenoid to measure the momentum of a muon, we must locate the center of the helical trajectory of the muon at the entrance and exit to the bent solenoid. This will be done by tracking detectors in the straight solenoid magnets on either side of the bent solenoid.

The reconstruction of helical trajectories in solenoid fields is a well established procedure, and we use results summarized in sec. 24.8 of the *Review of Particle Properties* (1996) to characterize the accuracy of such reconstruction. In particular, we suppose that the uncertainty on locating the center of the helix is the same as the uncertainty in measuring its radius of curvature. That is, we suppose that

$$\delta y_G = \delta R_{\rm curv} = R_{\rm curv}^2 \delta k, \tag{30}$$

where $k = 1/R_{\rm curv}$ is the curvature. The uncertainty δk is due both to uncertainty $\delta k_{\rm res}$ in the position measurements by the tracking device and to uncertainty $\delta k_{\rm ms}$ caused by multiple scattering. These two uncertainties can be approximated as

$$\delta k_{\rm res} = \frac{\sigma_{x,D}}{L^2 \sin^2\theta}\sqrt{\frac{720}{N}}, \tag{31}$$

and

$$\delta k_{\rm ms} = \frac{16\ [{\rm MeV}/c]}{LP\beta \sin^2\theta}\sqrt{\frac{L}{X_0}}, \tag{32}$$

for observation of $N \gg 1$ points on the trajectory over length L in a sampling medium (chamber gas) whose radiation length is X_0. The spatial resolution of each measurement is $\sigma_{x,D}$. Recall that θ is the angle between the muon trajectory and its guiding ray.

Labelling the ionization density in the chamber gas as n clusters/m so that $N = nL$, and recalling eq. (22) we then have

$$\delta y_{G,\mathrm{res}} = \left(\frac{P \sin\theta}{eB_s}\right)^2 \frac{\sigma_{x,D}}{L^2 \sin^2\theta} \sqrt{\frac{720}{nL}} = \left(\frac{P}{eB_s}\right)^2 \frac{\sigma_{x,D}}{L^{5/2}} \sqrt{\frac{720}{n}}, \tag{33}$$

and

$$\delta y_{G,\mathrm{ms}} = \left(\frac{P \sin\theta}{eB_s}\right)^2 \frac{16\ [\mathrm{MeV}/c]}{LP\beta \sin^2\theta} \sqrt{\frac{L}{X_0}} = \left(\frac{P}{eB_s}\right)^2 \frac{16\ [\mathrm{MeV}/c]}{P\beta} \sqrt{\frac{1}{LX_0}}. \tag{34}$$

We will design the detector so that the position-resolution term, (33), dominates the uncertainty in the measurement of the height of the guiding ray. (See sec. 2.5.6 for a caveat.) Then we can combine eqs. (29) and (33) to predict the accuracy of the momentum measurement:

$$\frac{\sigma_{P,D}}{P} \approx \frac{1}{\theta_{\mathrm{bend}}} \frac{P}{eB_s} \frac{\sigma_{x,D}}{L^{5/2}} \sqrt{\frac{720}{n}}. \tag{35}$$

As expected, the momentum resolution improves with increasing magnetic field. However, to lower the cost of the solenoid channel we will want to use as low a magnetic field as possible. The momentum resolution is improved by increasing θ_{bend} and by increasing the length L of the tracking system. It would not be possible to assemble a planar transport system with $\theta_{\mathrm{bend}} > \pi$; we will try to keep θ_{bend} around 1 radian. Since the resolution improves as $L^{5/2}$ the easiest way to compensate for a lower field is to use a longer length L.

2.5.5 Limit on Radiation Lengths in the Tracking Device

Once the tracking length L has been chosen, the requirement that $\delta y_{G,\mathrm{ms}} < \delta y_{G,res}$ implies a requirement on the radiation length of the chamber gas. From eqs. (33) and (34) we see that we need

$$X_0 > \frac{n}{720} \left(\frac{16\ [\mathrm{MeV}/c]}{P\beta}\right)^2 \frac{L^4}{\sigma_{x,D}^2}. \tag{36}$$

While this is not satisfied by an atmospheric pressure gas, it is easily satisfied by a low-pressure chamber gas.

2.5.6 Limit on Radiation Lengths in the Momentum Spectrometer

A more stringent limit on the amount of material comes from consideration of the effect of multiple scattering in the upstream tracking device on the trajectories of muons in the downstream tracking device.

Recall that in the bent solenoid channel with guiding dipoles, momentum measurement is based on reconstruction of the guiding ray of the helical orbit, and not simply on reconstructing the orbit itself. Expression (29) for the momentum dispersion can be rewritten to

give the uncertainty of the momentum measurement, $\delta P/P$, in terms of the uncertainty δy_G in the vertical displacement of the guiding ray in the bent solenoid:

$$\frac{\delta P}{P} = \frac{eB_s}{P}\frac{\delta y_G}{\theta_{\rm bend}}. \tag{37}$$

When a muon undergoes multiple scattering its angle θ to the guiding ray changes, which causes a change in the radius of curvature of the helical trajectory. From eq. (22) this change is

$$\delta_{R_{\rm curv}} = \frac{P}{eB_S}\delta\theta_{\rm ms}, \tag{38}$$

where the subscript ms stands for multiple scattering. As a consequence, the transverse position of the guiding ray of the muon's trajectory is displaced by $\delta_{R_{\rm curv}}$. We identify this with the uncertainty δy_G that enters eq. (37) to find

$$\frac{\delta P}{P} = \frac{\delta\theta_{\rm ms}}{\theta_{\rm bend}}, \tag{39}$$

independent of the strength of the solenoid magnets.

From the usual expression for the effect of multiple scattering on angle:

$$\delta\theta_{\rm ms} = \frac{13.6\ {\rm MeV}/c}{P\beta}\sqrt{N_X}, \tag{40}$$

where $N_X = L/X_0$ is the number of radiation lengths of material along the particle's path, we find the limit that

$$N_X < \left(\frac{(\sigma_{P,D}/P)P\beta\theta_{\rm bend}}{13.6\ {\rm MeV}/c}\right)^2, \tag{41}$$

to be compatible with a desired momentum resolution $\sigma_{P,D}/P$. For example, to measure the momentum of 165-MeV/c muons to an accuracy of $\sigma_{P,D}/P = 0.0014$ would require $N_X < 0.0002$ radiation lengths in the momentum spectrometer. To meet this requirement we will optimize the pressure in the tracking devices (sec. 2.6.7).

We may wish to use helium gas in the bent solenoids between the tracking devices. Then we could take the possibly optimistic view that the limit (41) is not a strict bound, but may be too severe for a detector system in which essentially all material is the sampling medium. Then the amount of multiple scattering is measured to some accuracy for each muon and the momentum analysis is less uncertain than implied by eq. (39). The results of sec. 2.5.4 give a flavor of the more sophisticated analysis that still needs to be performed.

2.6 Optimization of Detector Parameters

2.6.1 Scaling Law for Cost of Superconducting Solenoids

Green *et al.* [3] have made a fit to the cost of a large number of existing solenoid magnets in 1991 dollars as

$$\text{Cost [M\$]} = 0.52(U\ [\text{MJ}])^{0.66}, \tag{42}$$

where U is the stored energy in MJoules given by

$$U\ [\mathrm{MJ}] = \int \frac{B^2 dvol}{2\mu_0} \approx 2(B_s\ [\mathrm{T}]\ R_s\ [\mathrm{m}])^2 L_s\ [\mathrm{m}], \tag{43}$$

and R_s and L_s are the radius and length of the solenoid, respectively. The approximation in eq. (43) takes the total stored energy to be 1.6 times that within the cylinder of radius R_s and length L_s. Combining (42) and (43) we find

$$\mathrm{Cost}\ [\mathrm{M\$}] = 0.82(B_s\ [\mathrm{T}]\ R_s\ [\mathrm{m}])^{1.32}(L_s\ [\mathrm{m}])^{0.66}. \tag{44}$$

In the present application, the total length of the solenoid system (in contrast to the length of the tracking detector) depends only slightly on the details of the design of the experiment. Hence, to a first approximation the magnet cost is least after minimizing the product $B_s R_s$.

2.6.2 Minimum Solenoid Radius

We adopt the criterion that to keep beam-transport losses below 10^{-3} the solenoid radius R_s must be greater than $3.3\sigma_R$, where $\sigma_R = \sqrt{\sigma_x^2 + \sigma_{y\,\mathrm{max}}^2}$ is the maximum rms radial extent of the beam in the solenoid channel.

In this section we present an analysis of a straight solenoid, and add the effect of a bent solenoid in the next section.

If the beam enters the channel with transverse emittance ϵ_x and betatron parameter $\beta^\star$ then at a waist the rms transverse width is

$$\sigma_{x,\mathrm{waist}} = \sqrt{\epsilon_x \beta^\star}, \tag{45}$$

and rms angular spread

$$\sigma_{x',\mathrm{waist}} = \sigma_\theta = \sqrt{\frac{\epsilon_x}{\beta^\star}}. \tag{46}$$

As the muons leave the waist they travel in helices with radius of curvature $R_{\mathrm{curv}} \approx P\theta/eB_s$. The distribution of radii of curvatures than has rms width

$$\sigma_{R_{\mathrm{curv}}} = \frac{P}{eB_S}\sigma_\theta = \frac{P}{eB_S}\sqrt{\frac{\epsilon_x}{\beta^\star}}. \tag{47}$$

The maximum rms width, $\sigma_{x,\mathrm{max}}$, of the transverse motion can be estimated as the sum in quadrature of $\sigma_{x,\mathrm{waist}}$ and $\sigma_{R_{\mathrm{curv}}}$. This is minimized when the two terms are equal, which implies that we should chose $\beta^\star = P/eB_s$, leading to $\sigma_{R,\mathrm{max}} = \sqrt{2}\sigma_{x,\mathrm{max}} = 2\sqrt{P\epsilon_x/eB_s}$.

The preceding simplified argument can be formalized using the transfer matrix for a particle completely within a solenoid magnet:[2]

$$\mathbf{M} = \begin{pmatrix} 1 & \frac{P}{eB_s}\sin\phi & 0 & \frac{P}{eB_s}(\cos\phi - 1) \\ 0 & \cos\phi & 0 & -\sin\phi \\ 0 & -\frac{P}{eB_S}(\cos\phi - 1) & 1 & \frac{P}{eB_S}\sin\phi \\ 0 & \sin\phi & 0 & \cos\phi \end{pmatrix}, \tag{48}$$

[2]We have calculated this matrix ourselves. It is NOT the transfer matrix for a solenoid including fringe fields as found in TRANSPORT [4, 5].

where $\phi = eB_s\Delta z/P = 2\pi\Delta z/\lambda_B$. The transverse phase space of the beam is characterized by the beam matrix σ_{ij} where $i = x,\ x',\ y,\ y'$. The transformation of the beam matrix from position z_0 along the beam to position $z_1 = z_0 + \Delta z$ is given by

$$\boldsymbol{\sigma}^1 = \mathbf{M}\boldsymbol{\sigma}^{\mathbf{0}}\mathbf{M}^T, \tag{49}$$

where $\mathbf{M}^T$ is the transpose of matrix $\mathbf{M}$.

If we start from a waist, matrix $\boldsymbol{\sigma}^0$ is diagonal with $\sigma^0_{xx} = \sigma^0_{yy} = \sigma^2_x$ and $\sigma^0_{x'x'} = \sigma^0_{y'y'} = \sigma^2_{x'}$. We are presently interested in $\sigma^2_R = \sigma^1_{xx} + \sigma^1_{yy}$, which follows from eq. (49):

$$\begin{aligned}\sigma^2_R &= (M^2_{xx} + M^2_{xy} + M^2_{yx} + M^2_{yy})\sigma^0_{xx} + (M^2_{xx'} + M^2_{xy'} + M^2_{yx'} + M^2_{yy'})\sigma^0_{x'x'} \\ &= 2\epsilon_x\left(\beta^\star + 2\left(\frac{P}{eB_s}\right)^2\frac{1-\cos\phi}{\beta^\star}\right),\end{aligned} \tag{50}$$

using eqs. (45-46). We desire the conditions for which σ^2_R is a maximum with respect to ϕ but a minimum with respect to $\beta^\star$. Clearly the maximum in ϕ occurs at $\phi = \pi$, one half cylcotron period from the waist. Then

$$\frac{\partial\sigma^2_R(\phi=\pi)}{\partial\beta^\star} = 0 \qquad \Rightarrow \qquad \beta^\star\ [\mathrm{m}] = \frac{2P}{eB_s} = \frac{P\ [\mathrm{MeV}/c]}{150B_s\ [\mathrm{T}]}, \tag{51}$$

twice that found in the simplified argument. The corresponding rms width of the beam is $\sqrt{2}$ times that found by the simplified argument:

$$\sigma_{R,\max}\ [\mathrm{m}] = 2\sqrt{\frac{2P\epsilon_x}{eB_s}}. \tag{52}$$

2.6.3 Effect of a Bent Solenoid on the Minimum Radius

The argument of the preceding section holds in a bent solenoid only for the beam size in the x-direction, *i.e.*, in the horizontal bend plane. In the vertical direction (y) the momentum dispersion enlarges the beam according to eq. (29), so the channel must have a larger inner radius.

Furthermore, if the guiding dipole has a uniform field, expression (29) actually holds only for muons whose guiding ray enters the bent solenoid at $x = 0$. To see this, note that the field in the bent solenoid varies with x according to

$$B_s(x) = B_s(0)\frac{R_{\mathrm{bend}}}{R_{\mathrm{bend}} + x}, \tag{53}$$

taking positive-x as away from the center of curvature of the bent solenoid. (In this section we imagine the x-axis as perpendicular to the central ray.) Recall that eq. (29) expresses the difference of the curvature drift caused by the bent solenoid and the correction applied by the guiding dipole which is matched to the central momentum, P_0. That is, we can rewrite eq. (29) for a muon of momentum $P = P_0 + \Delta P$ whose guiding ray is has coordinate x as

$$y_G(x) \approx \left(\frac{P}{eB_s(x)} - \frac{P_0}{eB_s(0)}\right)\theta_{\mathrm{bend}} \approx \frac{P_0}{eB_s(0)}\left(\frac{\Delta P}{P_0} + \frac{x}{R_{\mathrm{bend}}}\right)\theta_{\mathrm{bend}}. \tag{54}$$

In practice the two terms in the rightmost form of eq. (54) would be comparable, leading to the need for an even larger bent solenoid to contain the beam.

Therefore, the guide field should not be uniform, but should vary with x in the same way as the bent solenoid field:

$$B_G(x) = B_G(0)\frac{R_{\rm bend}}{R_{\rm bend}+x}, \tag{55}$$

Then the vertical dispersion due to the bent solenoid will contribute only

$$\sigma_{y,\rm disp} \approx \frac{P}{eB_s}\frac{\sigma_P}{P}\theta_{\rm bend} \tag{56}$$

to the vertical beam size. In this expression, σ_P/P measures the momentum spread of the muon beam

This must be added in quadrature to the maximal beam size due to transport in a straight solenoid, eq. (52), to yield

$$\sigma_{R,\rm max} \approx \sqrt{\left(\frac{P}{eB_s}\frac{\sigma_P}{P}\theta_{\rm bend}\right)^2 + \frac{8P\epsilon_x}{eB_s}}. \tag{57}$$

Then our requirement that the solenoid radius R_s be at least $3.3\sigma_R$ leads to the quadratic equation

$$\theta_{\rm bend}\left(\frac{\sigma_P}{P}\right)^2\left(\frac{P}{eB_s}\right)^2 + 8\epsilon_x\frac{P}{eB_s} - \left(\frac{R_s}{3.3}\right)^2 = 0, \tag{58}$$

whose solution is

$$\frac{P}{eB_s} = \sqrt{\left(\frac{4\epsilon_x}{\theta_{\rm bend}(\sigma_P/P)^2}\right)^2 + \frac{1}{\theta_{\rm bend}}\left(\frac{R_s}{3.3(\sigma_P/P)}\right)^2} - \frac{4\epsilon_x}{\theta_{\rm bend}(\sigma_P/P)^2}. \tag{59}$$

2.6.4 Choice of Solenoid Parameters

From eq. (59) we see that the optimal product B_sR_s that enters in the magnet-cost parametrization (44) decreases as the magnet radius R_s increases. Hence in principle, the cost is minimized by a solenoid with arbitrarily weak field surrounding a beam of arbitrarily large size.

Therefore we must use some other criterion to set the beam size, which we see should be as large as is reasonable. A practical consideration in the present experiment is that the muon beam must fit through the $\rm TM_{0,1,0}$ RF timing cavity, whose radius is 14.6 cm at 800 MHz (see sec. 3). We chose

$$R_s = 10 \text{ cm} \tag{60}$$

so that the energy gain for a muon at radius R_s is still one half that of one on axis.

Many parameters of the solenoid channel can now be set based on previous considerations. The solenoid field follows from eq. (59):

$$B_s = \frac{P}{e\left[\sqrt{\left(\frac{4\epsilon_x}{\theta_{\rm bend}(\sigma_P/P)^2}\right)^2 + \frac{1}{\theta_{\rm bend}}\left(\frac{R_s}{3.3\sigma_P/P}\right)^2} - \frac{4\epsilon_x}{\theta_{\rm bend}(\sigma_P/P)^2}\right]}$$

$$= \frac{165}{300\left[\sqrt{\left(\frac{4\cdot 8\times 10^{-4}}{(0.05)^2}\right)^2 + \left(\frac{0.1}{3.3\cdot 0.05}\right)^2} - \frac{4\cdot 8\times 10^{-4}}{(0.05)^2}\right]} = 4 \text{ T} \tag{61}$$

for a beam of 165-MeV/c muons with transverse emittance of 800π mm-mrad and a momentum spread of $\sigma_P/P = 0.05$ in a bent solenoid channel with $\theta_{\text{bend}} = 1$ radian.[3]

The numerical simulations reported in sec. 2.6.5 indicate that we can confine the beam to 10 cm radius in a 3 Tesla field rather than 4 T as suggested by eq. (61). Hence we will provisionally adopt 3 T as the solenoid field strength.

The solenoid channel will consist of four sections, two upstream and two downstream, each about 4 m long. Then the cost per section is

$$\text{Cost} = 0.82(3 \cdot 0.1)^{1.32} \cdot 4^{0.66} = 0.42 \text{ M\$} \qquad (R_s = 10 \text{ cm}) \tag{62}$$

in 1991 dollars according to eq. (44).

It would be useful to increase the inner radius of the solenoid to about 15 cm to provide clearance for detector mounts. The cost for this option would be

$$\text{Cost} = 0.82(4 \cdot 0.15)^{1.32} \cdot 4^{0.66} = 0.71 \text{ M\$} \qquad (R_s = 15 \text{ cm}) \tag{63}$$

per magnet section.

The $\beta^\star$ for the solenoid channel should be

$$\beta^\star_{\text{optimal}} = \frac{P \text{ [MeV/}c\text{]}}{150 B_s \text{ [T]}} = \frac{165}{150 \cdot 3} = 0.367 \text{ m} \tag{64}$$

according to eq. (51).

The rms beam widths at a waist are then

$$\sigma_x = \sqrt{\epsilon\beta^\star} = 1.7 \text{ cm} \qquad \text{and} \qquad \sigma_{x'} = \sqrt{\epsilon/\beta^\star} = 47 \text{ mrad.} \tag{65}$$

The parameters of the optimized bent-solenoid channel are summarized in Table 2, which includes parameters for an option using a 400-MHz RF timing cavity as well.

2.6.5 Numerical Simulation of Beam Transport in the Solenoid Channel

We have performed a numerical simulation of the muon trajectories by integrating the equations of motion. At present we assume that the horizontal fields within the straight solenoid sections are those of an ideal solenoid, and those in the bent solenoids are those of an ideal toroidal sector. Likewise, ideal vertical guiding fields are superimposed on the bent solenoids. Thus Maxwell's equations are piecewise satisfied, but the fields suffer discontinuities at the boundaries between straight and bent solenoids.

Figure 4 shows the orbits of 200 muons selected at random from within the Gaussian phase volume specified in Table 2. The periodicity of the orbits with λ_B is readily evident in the upstream part of the 3-T solenoid channel, but is washed out due to chromatic effects by the end of the channel, which is about $7\lambda_B$ long.

[3] We use momentum spread of 0.05 rather than 0.03 as in Table 1 because the input beam to the FOFO cooling experiment should have a momentum-amplitude correlation that increases the total momentum spread.

Table 2: Parameters of the optimized bent-solenoid muon channels with 800- and 400-Mhz RF timing cavities.

Parameter	Value	Value
$F_{\rm RF}$	800 MHz	400 MHz
$P_{\rm muon}$	165 MeV/c	165 MeV/c
$B_{\rm Guide}$	0.55 T	0.55 T
B_s	3 T	1.5 T
$\theta_{\rm bend}$	1 rad	1 rad
$R_{\rm bend}$	1 m	1 m
λ_B	1.15 m	2.30 m
R_s	15 cm	24 cm
L_s	4 m	4 m
Cost per 4-m section	0.71M$	0.53M$
$\beta^\star$	36.7 cm	73.3 cm
$\sigma_x = \sigma_y$	17 mm	24 mm
$\sigma_{x'} = \sigma_{y'}$	47 mrad	33 mrad
$L_{\rm tracking}$	43 cm	57 cm
n	33 clusters/m	33 clusters/m

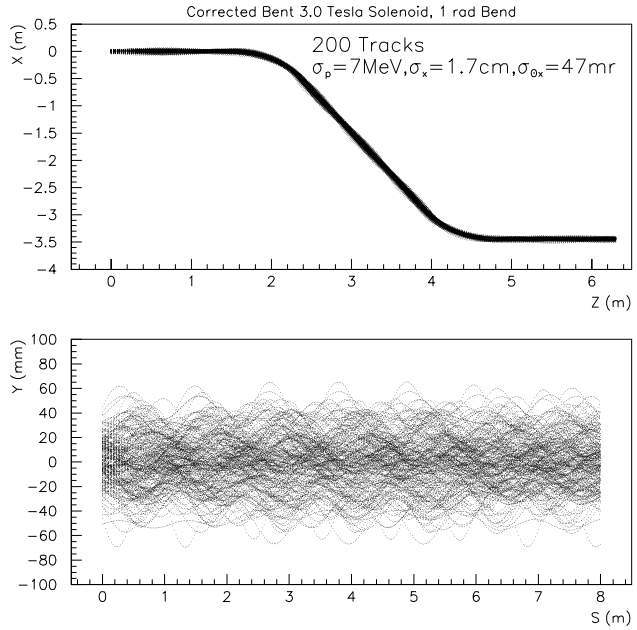

Figure 4: Orbits of 200 muons chosen at random from within the Gaussian phase volume specified in Table 2, projected onto horizontal and vertical planes as a function of position along a 3-T bent-solenoid muon channel. The Larmor wavelength, $\lambda_B = 1.15$ m, is evident in the upstream part of the channel.

Figure 5 shows the x and y profiles of the beam at the beginning, middle ($s = 3.5\lambda_B = 4.03$ m) and end ($s = 8$ m $= 6.96\lambda_B$) of a 3-T solenoid channel. The profiles broaden after the first bend due to the momentum dispersion, The second bend largely undoes the effects of the dispersion. We see that $\sigma_{R,\max} = \sqrt{\sigma_{x,\max}^2 + \sigma_{y,\max}^2} = 3.46$ cm.

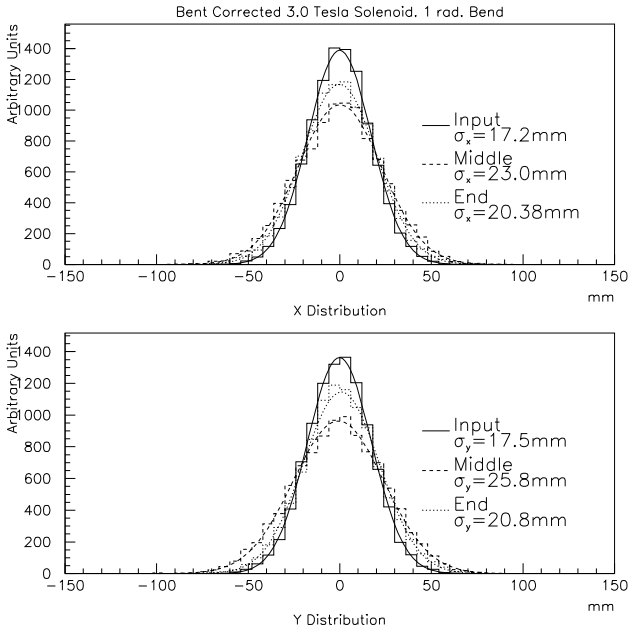

Figure 5: The distribution of muons along horizontal and vertical axes at the beginning, middle (= RF timing cavity) and end of the upstream 3-T bent-solenoid channel.

Figure 6 shows the radial profile of the beam at the same locations as in Fig. 5. The log plot shows that the beam is confined to $R < 10$ cm to better than one part per 1,000.

Figure 7(a) shows the trajectories of muons that lie along the central ray upstream of the first bend, but differ from the central momentum in increments of 1 MeV/c. The vertical dispersion caused by the bent solenoid is evident. Figure 7(b) shows the vertical displacement of the guiding ray or 200 random muons as a function of their momentum, in agreement with eq. (29). The small width of the diagonal band is an indication of a small x-dependence to the vertical momentum dispersion; this is caused by the 'grad-**B** force' that we have neglected in the analytic discussions.

Figure 8 shows the x and y profiles of the beam at the beginning, middle ($s = 1.5\lambda_B = 3.45$ m) and end ($s = 8$ m $= 3.48\lambda_B$) of a 1.5-T solenoid channel. The profiles broaden after the first bend due to the momentum dispersion, The second bend largely undoes the effects of the dispersion. We find that $\sigma_{R,\max} = \sqrt{\sigma_{x,\max}^2 + \sigma_{y,\max}^2} = 5.6$ cm.

Figure 9 shows the rms width, $\sigma_{y,\max}$ of the vertical profile of the beam at the middle ($s = 1.5\lambda_B = 3.45$ m) of a 1.5-T solenoid channel as a function of the input $\beta^\star$. The minimum of $\sigma_{y,\max}$ occurs near $\beta^\star = 73$ cm, which confirms eq. (51) for the optimized $\beta^\star$ as a function of solenoid field.

Figures 5, 6 and 8 indicate that the rms x and y beam sizes have increased somewhat during transport in the bent solenoid system. Likewise, the rms sizes of the x and y mo-

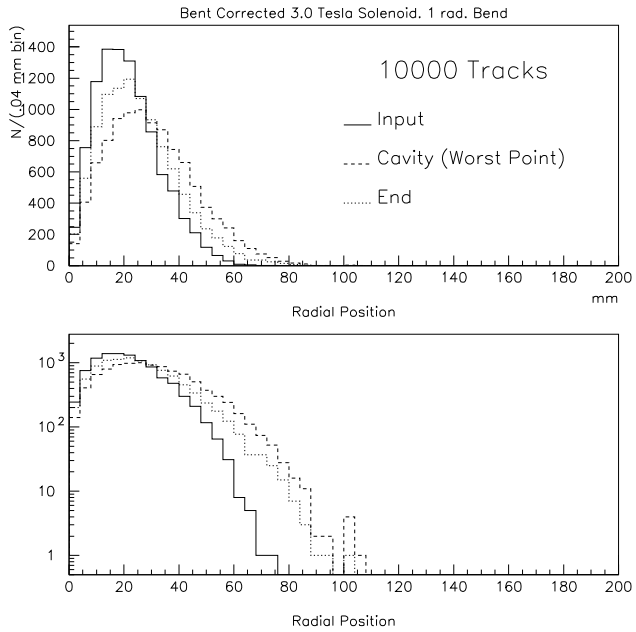

Figure 6: The radial distribution of muons the beginning, middle (= RF timing cavity) and end of the upstream 3-T bent-solenoid channel.

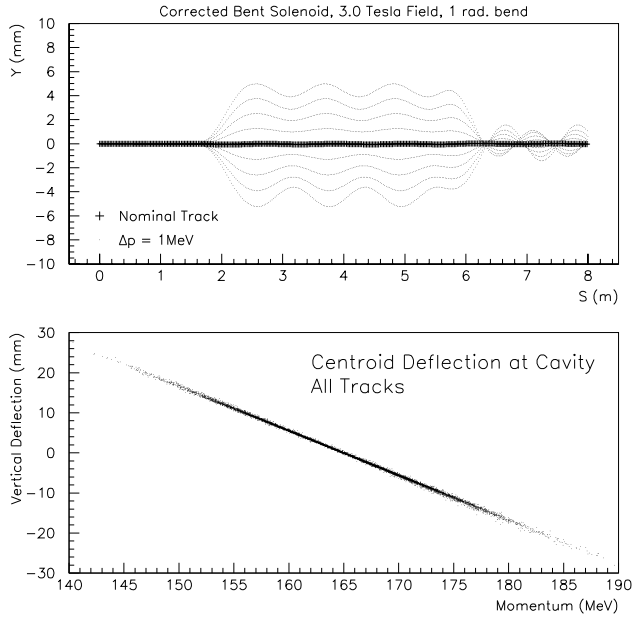

Figure 7: (a) Vertical projection of trajectories of muons that lie along the central ray upstream of the first bend of a 3-T solenoid channel, but depart from the central momentum by 1-MeV/c increments. The first bend covers the interval $s = [1.5, 2.5]$ m and the second covers [5.5,6.5] m. The vertical momentum dispersion between the bent solenoids is evident. (b) Summary of vertical deflection of the guiding ray of muons as a function of their momentum. Compare to eq. (29).

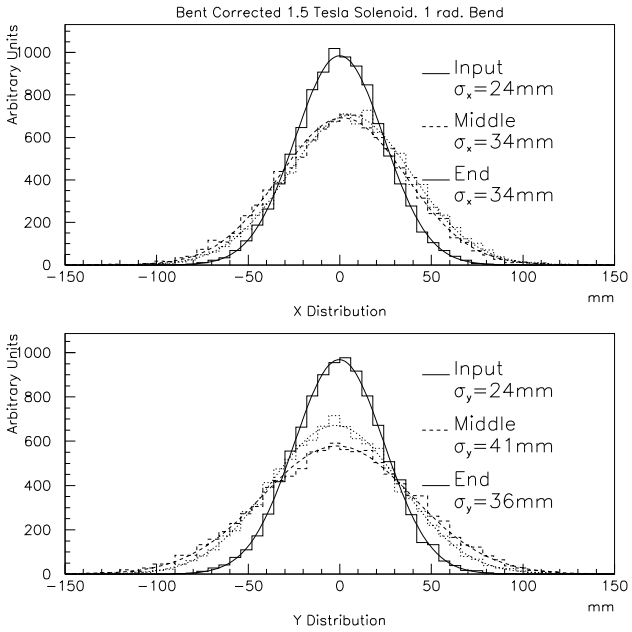

Figure 8: The distribution of muons along horizontal and vertical axes at the beginning, middle (= RF timing cavity) and end of a 1.5-T bent-solenoid channel.

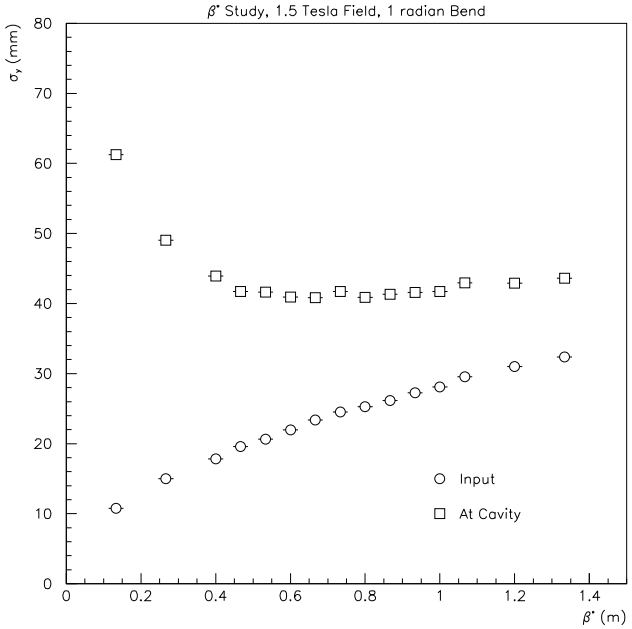

Figure 9: The rms width of the distribution of muons along the vertical axis at the middle (= RF timing cavity) of a 1.5-T bent-solenoid channel as a function of $\beta^\star$. The input width is $\sqrt{\epsilon_x \beta^\star}$ with $\epsilon_x = 800\pi$ mm-mrad.

mentums components will grow slightly, as shown in Fig. 10. Thus the transverse emittance appears to have grown if it is calculated according to

$$\epsilon_\perp = \sigma_x \sigma_y \sigma_{P_x} \sigma_{P_y}. \tag{66}$$

Indeed, by this measure, $\epsilon_{\perp,\mathrm{in}} = 1.72 \cdot 1.75 \cdot 7.84 \cdot 7.69 = 181.5$ (cm-MeV/c)^2, while $\epsilon_{\perp,\mathrm{out}} = 2.04 \cdot 2.08 \cdot 8.02 \cdot 8.06 = 274.3$ (cm-MeV/c)^2,

However, since there is no dissipation in our model the total phase volume is conserved. The shape of that volume is, however, distorted from the ellipsoid aligned along the coordinate axes as assumed in eq. (66). A first measure of the distortion can be obtained by examining the off-diagonal second moments, such as $\sigma^2_{xy} = \langle xy \rangle$. Among the six such moments involving the four transverse-phase-space variables, only $\sigma^2_{xP_y} = 6.25$ cm-MeV/c and $\sigma^2_{yP_x} = 6.11$ cm-MeV/c are significantly nonzero at the end of the bent-solenoid transport, as shown in Fig. 11. A better estimate of the transverse emittance is then [6]

$$\epsilon_{\perp,\mathrm{out}} = \sqrt{(\sigma_x^2 \sigma_{P_y}^2 - \sigma_{xP_y}^4)(\sigma_y^2 \sigma_{P_x}^2 - \sigma_{yP_x}^4)} = 233.3 \text{ (cm-MeV/}c\text{)}^2. \tag{67}$$

About half the apparent emittance growth is accounted for in the first correction.

The apparent emittance growth is large for lower magnetic fields in the solenoid channel.

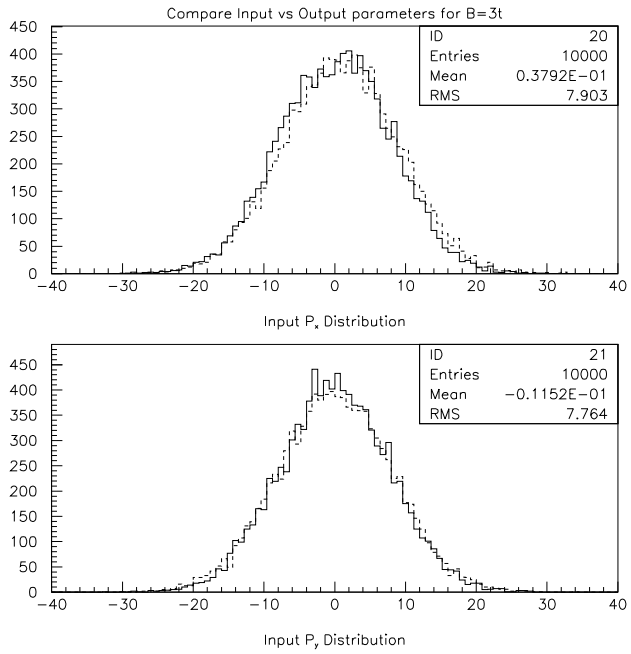

Figure 10: Distributions of x and y components of the muon momenta at the beginning and end of a 3-T bent solenoid channel.

2.6.6 Remarks on Weighted Sampling Strategies

The apparent emittance growth in the bent-solenoid channel leads us to some general reflections on strategies.

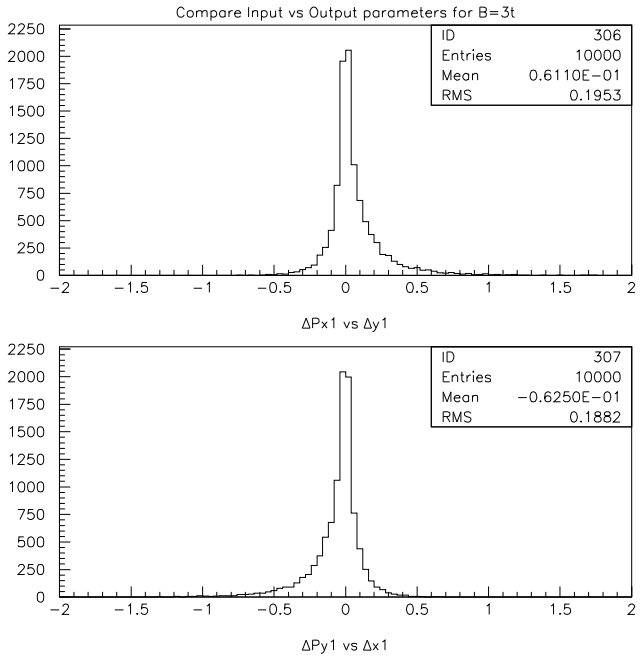

Figure 11: Distributions of xP_y and yP_x at the end of a 3-T bent solenoid channel. The means of the distribution are the off-diagonal 2nd moments $\sigma^2_{xP_y}$ and $\sigma^2_{yP_x}$. The units are m-MeV/c.

We must deliver a set of muons with a specified normalized emittance, represented by, say, $\epsilon_{x,N} = 1500\pi$ mm-mrad, to the cooling experiment. We do not necessarily have to accept a beam of that emittance at the entrance to the upstream solenoid channel.

For example, we could start with a smaller emittance and let it 'grow' to to the specified emittance. Since it costs more to contain a beam of larger initial emittance, this might be a useful strategy.

Because we propose to analyze individual muons and build up a 'beam' in software, we have even more freedom along these lines.

In particular, we don't have to achieve a perfect, uncorrelated Gaussian distribution of particles in 6-D phase space. If the actual phase-space distribution of our muons has the wrong shape, we can weight muon by muon to achieve the desired shape – so long as we transmit a reasonably representative sample of muons.

If we want an experiment with 10,000 selected muons, and also want to keep track of losses in the cooling apparatus to 1 part per 1,000, then no weight should be larger than 10 (compared to the average weight).

In the previous section we found in a simulation that the apparent emittance of the beam increased by a factor of 1.5 in the solenoid channel. The larger apparent emittance indicates that the density in phase volume is no longer as smooth as desired, but varies only by factors of order 1.5 from an ideal uncorrelated distribution. We can apply software weights to simulate the ideal bunch without undue risk of underrepresentation in any region of phase space.

There are other implications of such a selection strategy. Whether or not we use weights we will have to collect more than 10,000 muons to select a subset of 10,000 that populate phase volume in our desired manner.

A sense of this can be gotten from an argument based on time-reversal invariance. Suppose we desired a set of completely uncorrelated muons at the output of the solenoid channel (input to cooler) with a phase-space density ρ_1 that has emittance ϵ_1. Then our present study can be used to tell us what the input distribution must be. We know from the simulation that an input distribution $\{\rho_1, \epsilon_1\}$ propagates to an output distribution $\{\rho_2, \epsilon_2\}$, calculating the 'apparent' emittance ϵ_2 according to eq. (66). Since $F = ma$ is time-reversal invariant, if we started with the distribution $\{\rho_2, \epsilon_2\}$ but reversed all velocities ($x' \to -x'$, $y' \to -y'$), then distribution $\{\rho_2, \epsilon_2\}$ would propagate into distribution $\{\rho_1, \epsilon_1\}$ (with velocities reversed).

In practice we could not arrange the input beam to have substructure such that the 'true' emittance is ϵ_1 but the apparent emittance is $\epsilon_2 > \epsilon_1$. Instead, we would have to prepare a beam with 'true' emittance ϵ_2; this would guarantee that the output beam would contain muons sufficient to form a bunch of emittance ϵ_1 with no weighting. But a bunch with 'true' emittance ϵ_2 contains more particles than the bunch of 'apparent' emittance ϵ_2 which happens to evolve into a bunch with 'true' emittance ϵ_1.

The price of using unit weights will be both longer running time and higher magnet costs than is the case for a well-chosen weighting strategy.

2.6.7 Optimization of Tracking-Device Parameters

The length of each tracking detector is set by eq. (35) to be

$$L_{\text{tracking}} = \left(\frac{1}{\theta_{\text{bend}}} \frac{P}{eB_s} \frac{\sigma_{x,D}}{\sigma_{P,D}/P} \sqrt{\frac{720}{n}} \right)^{0.4} . \tag{68}$$

The number of radiation lengths in the tracking device is proportional to nL_{tracking}, which should satisfy the limit (41). From eq. (68) we see that L_{tracking} varies as $n^{-0.2}$, *i.e.*, very slowly with the ionization density n. Hence it is favored to reduce the ionization density as much as possible, compatible with the chamber still being able to produce gas gain, in exchange for a slightly longer tracking device.

We propose to use ionization density $n = 33$ cluster/m (3 cm between clusters). This can be achieved in 10-Torr methane, for example. Then eq. (68) sets the tracking length as

$$L_{\text{tracking}} = \left(\frac{165 \cdot 2 \times 10^{-4}}{3 \cdot 300 \cdot 1 \cdot 0.0014} \sqrt{\frac{720}{33}} \right)^{0.4} = 43 \text{ cm}, \tag{69}$$

assuming the solenoid bend angle is 1 radian, the detector spatial resolution is 200 μm and that the desired momentum resolution is $\sigma_{P,D}/P = 0.0014$. The number of radiation lengths in the methane gas of each tracking device would then be 0.000015, in compliance with eq. (41).

The Larmor period for 165-MeV/c muons at $B_s = 3$ T is $\lambda_B = 115$ cm, so each tracking detector observes the helix over an azimuth of 2.3 radians.

Table 3: Required detector resolution to achieve measurement accuracy of 1% on the rms widths σ_i, assuming the detector resolution function is known to 20%, *i.e.*, $\delta_{\sigma_D}/\sigma_D = 0.2$.

Parameter	Value
$\sigma_{x,D} = \sigma_{y,D}$	200 μm
$\sigma_{x',D} = \sigma_{y',D}$	5 mrad
$\sigma_{P,D}/P$	0.0014
$\sigma_{z,D}$	2 mm
$\sigma_{t,D}$	8 ps

2.7 Summary of Detector Requirements

The cooling apparatus is designed for a momentum acceptance of $\sigma_P/P = 3\%$. Simulations indicate that cooling of transverse emittance $\epsilon_{N,x} \approx 1500\pi$ mm-mrad is achieved for input bunch lengths only up to $\sigma_z \approx 1$ cm. While the cooling apparatus reduces the transverse emittance, the longitudinal emittance is expected to increase slightly, corresponding to output bunch length of $\sigma_z = 1.2$ cm.

The criterion (14) that the detector resolution $\sigma_{i,D}$ be less than 20% of the rms width σ_i of phase-space parameter i is in some cases less restrictive than that required to extrapolate the time measurement from the detector to the ends of the cooling apparatus. Table 3 summarizes the requirements on detector resolution found in the several preceding arguments.

2.8 Measurement of the Detector Resolution

An important preliminary step in the cooling experiment is the determination of the various detector resolutions $\sigma_{i,D}$ and associated uncertainties $\delta_{\sigma_{i,D}}$ needed to implement the analysis according to eq. (8). A powerful technique for this would be the use of the 'after' arm of the experiment to study the 'before' arm, and *vice versa*. To implement this the experiment should be initially commissioned without the cooling apparatus present, and the two arms should initially be positioned with no gap between them.

It seems likely that the relative uncertainty in detector resolution, $\delta_{\sigma_D}/\sigma_D$ can be reduced to much less than the 20% assumed above.

3 $TM_{0,1,0}$ RF Timing Cavity

The conventional techniques of time measurement in high-energy physics have uncertainties that are large compared to the desired resolution of 8 ps. In sec. 5 we consider an improvement in 'conventional' timing methods that might be useful as an auxiliary measurement. To attain the desired resolution we have examined the use of RF cavities that transform time offsets into position, angle or energy (momentum) offsets, following initial studies by Rick

Fernow. Such techniques have been considered earlier by Haimson [7]. We presume the RF timing cavity would operate at the same frequency as does the cooling apparatus, namely 800 MHz.

We first considered a $TE_{0,1,1}$ cavity which displaces the beam in x without changing its angle [8]. However, the displacement is quite small, only 6 μm/ps over a length of 20 cm with a peak field of 40 MV/m in the cavity. A measurement of this displacement would be limited by the uncertainty in the extrapolation of the trajectory across the cavity. The displacement of 6 μm/ps corresponds to an angle of 30 μrad/ps across the cavity, which is minute compared to the angular uncertainty of 6 mrad that can be tolerated in measurement of the other phase-space coordinates.

We next considered a $TM_{2,1,0}$ cavity which deflects the angle of the beam by 90 μrad/ps, *i.e.*, about three times the effective deflection of the $TE_{0,1,1}$ cavity [9]. This effect is still very marginal.

An alternative scheme to determine the longitudinal position of a muon with the bunch is to measure its momentum, accelerate it in a cavity phased to null at the center of the bunch, and measure the momentum again [10]. The momentum difference is then proportional to the longitudinal position. This scheme gives results that are independent of the amount of multiple scattering in the RF cavity. As shown below, straggling will not present a problem either. The required momentum resolution is comparable to that desired for the momentum measurement by itself. It would be even more advantageous to use a 4- or 8-cell accelerating cavity of the same design as for the FOFO cooling section, but phased by 90°.

3.1 Cylindrical $TM_{0,1,0}$ Cavity Fields

The rf cavity is centered on $(x, y, z) = (0, 0, 0)$, and is a cylindrical can of radius a and length b along the beam direction z.

The trajectory of a typical beam particle for the cavity field OFF is parametrized as

$$\begin{aligned} x &= x_0 + \beta_x ct, \\ y &= y_0 + \beta_y ct, \\ z &= z_0 + \beta_z ct, \end{aligned} \tag{70}$$

where c is the speed of light. The beam axis is the z-axis:

$$\beta_x,\ \beta_y \ll \beta_z, \qquad \text{and} \qquad \beta_z \approx \beta. \tag{71}$$

We will make the impulse approximation that the cavity fields do not affect the muon trajectories in y or z, but only in x. Thus we assume the y and z parametrizations in (1) also hold when the field is on.

The particle is within the cavity during the interval

$$[t_{\min}, t_{\max}] = \left[-\frac{b}{2\beta_z c} - \frac{z_0}{\beta_z c}, \frac{b}{2\beta_z c} - \frac{z_0}{\beta_z c} \right]. \tag{72}$$

The wave equation tells us that for a cylindrical $TM_{0,1,0}$ cavity of radius a, diameter d and length b along the z-axis,

$$\frac{\omega}{c} = \frac{2.405}{a}, \qquad \text{so} \qquad d = 2a = \frac{2.405}{\pi}\lambda = 0.766\lambda. \tag{73}$$

The fields in the cylindrical cavity whose electric field vanishes at $t = 0$ are (in Gaussian units)

$$\begin{aligned} E_r = E_\phi &= 0, \\ E_z &= E_0 J_0\left(\frac{2.405r}{a}\right)\sin\omega t, \\ B_\phi &= E_0 J_1\left(\frac{2.405r}{a}\right)\cos\omega t, \\ B_r = B_z &= 0. \end{aligned} \tag{74}$$

3.2 Energy Gain: Leading Approximation

The gain in energy, ΔU, when a muon traverses the cavity is

$$\begin{aligned} \Delta U &= e\int E_z dz = e\beta_z c\int_{t_{\min}}^{t_{\max}} E_z dt = e\beta_z c E_0 \int_{t_{\min}}^{t_{\max}} J_0\left(\frac{2.405r}{a}\right)\sin\omega t\, dt \\ &\approx e\beta_z c E_0 \int_{t_{\min}}^{t_{\max}} \sin\omega t\, dt = \frac{\beta_z c e E_0}{\omega}\left(\cos\omega t_{\min} - \cos\omega t_{\max}\right) \\ &\approx -\frac{\beta_z c e E_0}{\omega}\frac{2\omega z_0}{\beta_z c}\sin\frac{\omega b}{2\beta_z c} = -2eE_0 z_0 = -2eE_0\beta_z c\Delta t, \end{aligned} \tag{75}$$

using eq. (72) and supposing that the transverse size of the beam is small compare to a. In eq. (75) we have put $b = \beta_z\lambda/2$ to maximize ΔU.

From eq. (75) we see that ΔU depends on the x and y positions and slopes only in second order.

For a peak field of $E_0 = 40$ MV/m, and 165 MeV/c muons for which $\beta_z = 0.84$, we have

$$\Delta U = 0.02\ [\text{MeV}]\left[\frac{\Delta t}{1\ \text{ps}}\right]. \tag{76}$$

Since $U\Delta U = c^2 P\Delta P$, the energy gain corresponds to a relative momentum change

$$\frac{\Delta P}{P} = \frac{2eE_0\beta_z c\Delta t}{\beta c P} = \frac{2\cdot 40\ [\text{Mv/m}]\cdot 3\times 10^{-4}\ [\text{m/ps}]\cdot\Delta t\ [\text{ps}]}{165\ [\text{MeV}/c]\cdot c} = 0.00014\left[\frac{\Delta t}{1\ \text{ps}}\right]. \tag{77}$$

3.3 Discussion

It would be advantageous to use a 4- or 8-cell accelerating cavity of the same design as for the FOFO cooling section. Present parameters for these structures are a length of $b = \lambda\beta_z/3 =$ 10.5 cm per cell, and inner radius 14.6 cm. Because each cell is only 2/3 of the length we assumed in eq. (75) the timing correlation per cell is reduced by $\sin(60^\circ) = 0.866$. The total correlation over, say, 8 cells is then

$$\frac{\Delta P}{P} = 8\cdot 0.87\cdot 0.00014 = 0.001\left[\frac{\Delta t}{1\ \text{ps}}\right]. \tag{78}$$

Thus we would require a momentum resolution of $\sigma_P/P = 0.008$ to achieve a timing resolution of 8 ps $= 0.2\sigma_t$, in line with our general goal for all six phase-space parameters.

3.4 Straggling

An advantage of the timing measurement via an accelerating cavity is that multiple scattering within the RF cavity does not affect the time resolution. [Multiple scattering in the momentum spectrometer is, of course, a limiting factor in the momentum resolution.] However, the timing resolution will be degraded by straggling in the cavity walls and surrounding detectors. An approximate expression for momentum straggling [Rossi, *High Energy Particles*, p. 31, eqs. (8) and (9) with $E'_{\rm max} \approx 2\gamma^2\beta^2 m_e c^2$] is

$$\sigma_{P,\rm straggling} = \frac{\gamma r_e m_e c^2}{\beta c}\sqrt{2\pi N_0 \frac{Z}{A} s\left(1-\frac{\beta^2}{2}\right)} \approx 0.43\ [\rm MeV/\mathit{c}]\sqrt{\left[\frac{s}{1\ \rm g/cm^2}\right]}, \qquad (79)$$

where r_e is the classical electron radius, N_0 is Avagadro's number and s is the amount of material. The numerical result holds for $Z/A = 1/2$, and $\beta = 0.84$.

The momentum smearing due to straggling should be small compared to the desired resolution, *i.e.*, small compared to $\sigma_{P,D} = 0.006P = 1$ MeV/c for $P = 165$ MeV/c. Then the total material in the walls of the timing cavity plus surrounding chambers must satisfy

$$s < \left(\frac{\sigma_{P,D}}{0.43}\right)^2 = \left(\frac{1}{0.43}\right)^2 = 5\ [\rm g/cm^2]. \qquad (80)$$

This places very little constraint on the choice of materials.

3.5 The Need for an Auxiliary Timing Measurement

The linear correlation between time offset and momentum change given in (77) holds only for muons within about $\pm\lambda/8$ of the desired bunch center. The general relation is that the momentum change varies as $\sin(2\pi t/T)$ where T is the RF period. Thus the interpretation of the momentum offset becomes ambiguous for muons with t not near nT.

To remove this ambiguity there must be an auxiliary time measurement that locates the time to $\approx T/4 = 300$ ps. This is achievable by relatively 'conventional' techniques, as will be discussed in sec. 7.

4 The Tracking Time Projection Chambers

Multiple scattering in the material of the tracking system will limit its performance in measuring the angles, and hence momenta of the low-momentum muons in the cooling experiment. From eq. (41) we concluded that the nominal goal of a momentum resolution of $\sigma_P/P = 0.0014$ can be achieved only if the relevant material contains less than 0.0002 radiation lengths. Since one meter of air contains about 0.003 radiation lengths the tracking detector will have to be very low mass by usual standards.

Therefore we are exploring a design in which the entire beam-transport region is held at low pressure and filled with a gas such as methane, ethane or isobutane that is suitable for gas amplification of ionized electrons.

Low-pressure gas tracking devices appear to have been introduced by Binon *et al.* [11] (in consultation with Charpak), and have long been championed by Breskin [12]-[18]. They

have been studied at Fermilab by Anderson [19, 20] and by the present authors as well [21]. Low-pressure hydrocarbon gases are preferred over noble gases because of the superior stability of the former against UV-photon feedback.

4.1 Gas Gain

We anticipate the need to operate the TPC with a gas gain of 10^5 (signal/preamp noise $\approx 20:1$, which will permit good interpolation in space and time via charge sharing). Figures 12 and 13 show gain spectra of single-photoelectron avalanches a proportional chamber with a wire anode and filled with CH_4 or C_2H_6 gas. The technique of producing single-photoelectron avalanches via a 1-ns pulse from a N_2 laser incident on an aluminum cathode has been described by us in ref. [21].

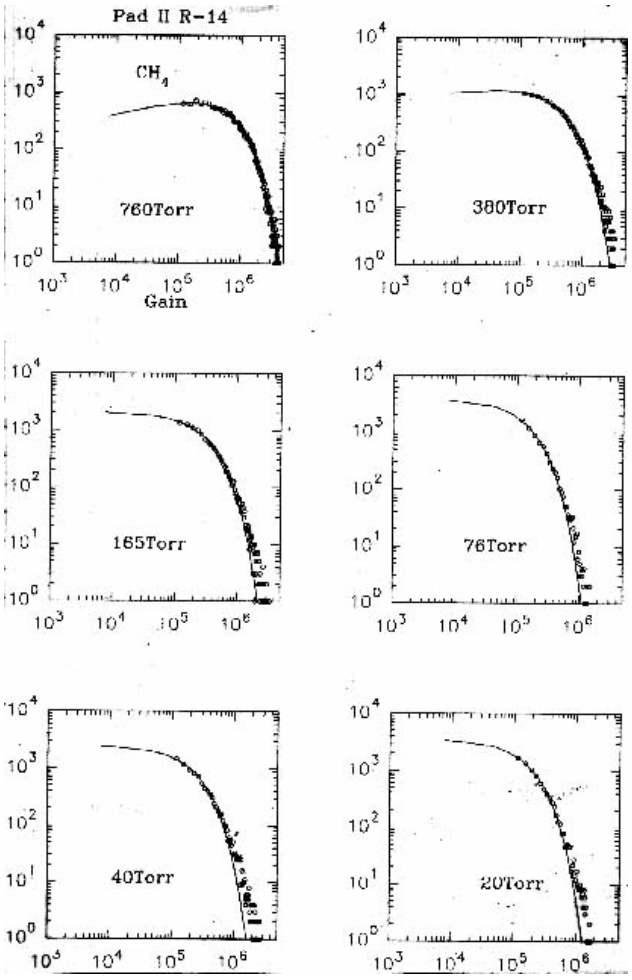

Figure 12: Gain spectra for single-photoelectron avalanches in CH_4 gas at various pressures.

At low pressure, the gain sprectrum in methane does not show a clear peak, and chamber operation is unstable at high gas gains. We interpret this behavior as due to the high

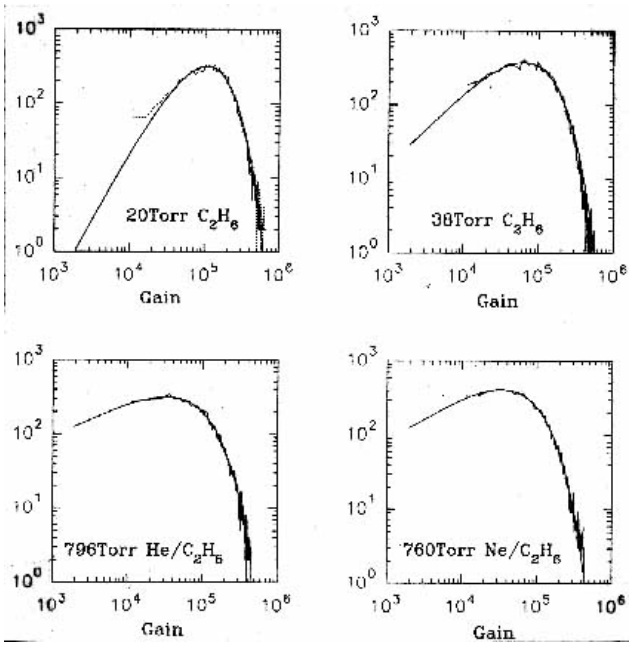

Figure 13: Gain spectra for single-photoelectron avalanches in C_2H_6, and He/C_2H_6 mixtures at various pressures.

probability of secondary avalanches in methane initiated by UV photons from the primary avalanche. Both ethane and isobutane have better "quenching" of the UV photons and show gain spectra with peaks, corresponding to more stable chamber operation. A related feature is that a lower voltage is required to achieve a given effective gain in methane than in ethane or isobutane, due to the larger contribution of secondary avalanches in the former gas.

If the tracking chambers can be operated near room temperature, an interesting option would be a helium/isobutane mixture, such as 90/10, which has good gain characteristics for very low total gas pressure.

4.2 Ionization Density

The ionization density by minimum ionizing particles in atmospheric-pressure methane, ethane and isobutane has been reported by Va'vra [22] as 25, 41, and 84 primary clusters per cm, respectively. A 165-Mev/c muon ionizes at about 1.2 times minimum, so the primary ionization density would be 30, 49 and 100 clusters/cm for the three gases. If we desire an average of one primary cluster per 3 cm in our low-pressure tracking device, as argued in sec. 2.6.5, the chamber pressure could then be 8.4, 5.2 or 2.5 Torr for the three gases (at 20°C).

These and other parameters of the low-pressure gases are summarized in Table 4.

At pressures below 10 Torr methane is still a gas at 77°K, liquid-nitrogen temperature. To save on operating costs of the superconducting solenoid channel it is favorable to run the detector near liquid-nitrogen temperature, which indicates methane to be the preferred chamber gas.

Table 4: Parameters for ionization of hydrocarbon gases at low pressure by 165-MeV/c muons.

Parameter	Methane	Ethane	Isobutane
Atomic number	16	30	58
Primary clusters/cm (1 atm., 20°C	30	49	100
Pressure (Torr, 20°C)	8.4	5.2	2.5
Pressure (Torr, 77°K)	2.2	–	–
Primary clusters/cm	1/3	1/3	1/3
Boiling temp. (°K, 1 atm.)	112	185	231
Boiling temp. (°K, 10 Torr)	77.7	130	195
Boiling temp. (°K, 1 Torr)	67.3	114	172
Radiation lengths/m	0.000017	0.00002	0.00002
Saturation E field (V/cm)	10	8.8	6
Saturation drift velocity (μm/ns)	100	50	40
Drift time over 45 cm (μsec)	4.5	9.0	11.25

The ionization density is, strictly speaking, a function of the gas density, not pressure. To maintain a given ionization density while lowering the temperature, the pressure should be reduced so P/T remains constant. Thus the ionization density of 1/3 per cm in methane at 77°K requires a pressure of only 2.2 Torr.

4.3 Radiation Lengths and Momentum Resolution

The number of radiation lengths per meter at these low pressures (strictly, low gas densities) would then be 0.000017, 0.00002 and 0.00002 for methane, ethane and isobutane, respectively. The momentum resolution would then be limited to $\sigma_P/P = 0.0007$ according to expression (41) for any of the three gases, assuming the chamber gas occupies the entire over 2.5-m length of the spectrometer. Thus we can achieve momentum resolution about two times better than the baseline goal of Table 3.

4.4 The Drift Velocity

The drift velocity of ionized electrons is a function of E/P where E is the applied electric field and P is the gas pressure.[4] The saturation drift velocity is independent of pressure, but is achieved for very low electric fields at low pressures, as can be inferred from Fig. 14.

Thus if we operate with 8.4-Torr methane the drift velocity would saturate at 100 μm/ns at a field of 10 V/cm. For ethane at 5.2 Torr the saturation drift velocity is 50 μm/ns at a field of 8.8 V/m, and for isobutane at 2.5 Torr the saturation drift velocity is 40 μm/ns at a field of 6 V/m.

[4]Strictly, the dependence of drift velocity is on E/N where N is the density. It is convenient to calculate the drift velocity using data at 20°C.

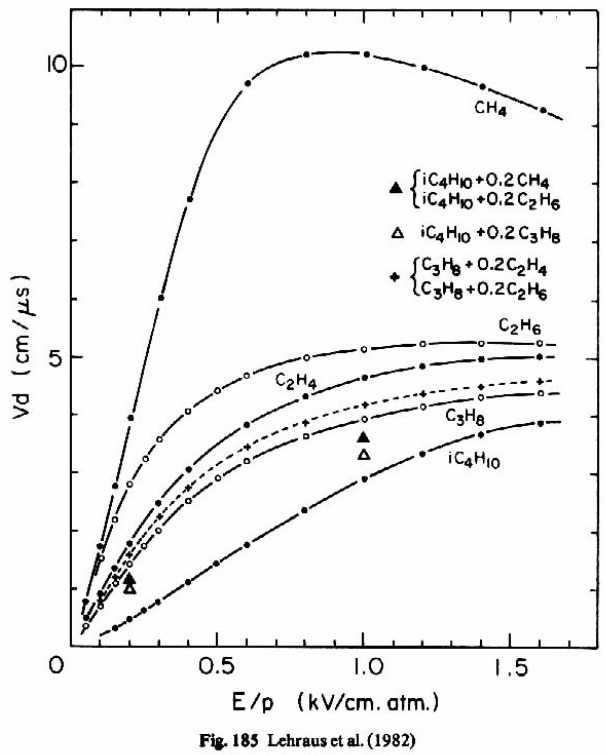

Figure 14: Drift velocity of electrons in hydrocarbon gases as a function of the reduced electric field E/P. From ref. [23].

4.5 The Time Projection Chamber

We have chosen a gas pressure so as the yield one primary ionization cluster per 3 cm of the muon trajectory. For good fitting of the helical tracks in the solenoid magnetic field there should be at least 10 clusters per track segment. Indeed, eq. (69) indicates that an optimized tracking device with this ionization density should be 45 cm long, providing 15 samples per track.

The tracking device must reconstruct the helical orbit of the muons in the solenoid field. In particular, the coordinates of the guiding ray of that helix must be measured. This requires similar accuracy in the measurement of both transverse coordinates.

A natural configuration of the tracking detector is then for the ionized electrons to drift along the magnetic field lines to be observed at a plane of x-y pads perpendicular to the magnetic field. The chamber electric field is then parallel to the magnetic field. This detector configuration can be called a time projection chamber, and is shown in Fig. 3.

The collection electrode would be on the end of the detector away from the bent solenoid, so multiple scattering in this electrode would have no influence on the momentum measure. However, the TPC geometry would then require a field-shaping cathode on the end of the chamber towards the bend. For simplicity of construction, this cathode should be a thin foil. Then the foil should be less than 0.000017 radiation lengths thick = radiation lengths in 1 m of the chamber gas. A 5-μm-thick beryllium foil would suffice.

An alternative chamber geometry could involve the electric field transverse to the magnetic field. This would have the advantage the no chamber electrode need intercept the beam. Flat electrodes 20 cm wide, 45 cm long and 20 cm apart would just fit inside the proposed 15 cm inner radius of the solenoid channel. The Lorentz angle of the drifting electrons would be large, and there would be some inherent difference in the quality of the x and y reconstruction. Because the 3-dimensional helix must be reconstructed, both x and y coordinates must be measured simultaneously. Thus a pad readout is again required, with a similar channel count as for the TPC. Also, a compact geometry along the beam axis would required foils with graded-potential electrodes perpendicular to the beam at the ends of the chamber.

Continuing with the discussion of the TPC option, in the anode region of the detector we must achieve gas amplification and signal pickup with good sensitivity to both x and y position. And of course, the readout must be capable of sampling in time during the arrival of the various clusters created along the trajectory.

A simple electrode configuration is shown in Fig. 3. The low-electric-field drift region is terminate by a transparent wire mesh grid. For example, stainless-steel wire mesh with 250-μm pitch and 80% (or even 90%) transparency is commercially available. The anode is a wire mesh of the same type, separated from the grid by a gap of a few mm. A voltage of less than 1000 V between the grid and anode will permit gas gain of up to 10^6, as shown in Fig. 15 from ref. [14].

Since the anode-mesh pitch is 250 μm, an rms transverse position resolution of 100 μm is possible, if the readout is sufficiently sensitive. To maintain this resolution for clusters that have drifted up to 45 cm, the drift path of the electrons must be well understood. This will be best insured if the active drift volume is in a region of very uniform magnetic field. Thus the detectors should be in straight solenoid sections and at least one solenoid diameter away from ends and transitions. To match the solenoid beam optics, we place the TPC's about 50 from the end of the straight solenoids. Then the central path length in each momentum spectrometer is 2.5 m.

Should gas gains in the range 10^6-10^8 be desirable, a so-called multistep electrode configuration could be used, as shown in Fig. 16 from ref. [18]. A short drift section (transfer gap) after the first amplification gap permits the avalanche to diffuse transversely before encountering the second amplification gap. The broader avalanche is less prone to UV-photon feedback instabilities and can be brought to higher gain.

4.6 Cathode Pad Plane

The signal is not read directly from the anode. Instead the signal is based on the charge induced on a segmented cathode pad plane a few mm from the anode. We anticipate a channel count of about 1250 pads in each of the eight TPC's, for a total of 10,000 readout channels. For example, if the pad-plane radius is 10 cm, each pad would be 5×5 mm^2 in area.

To achieve a transverse position resolution of 200 μm, the cluster centroid must then be determined to 1/25 of the pad width. This can be achieve by measurement of charge sharing on the pads. Modelling [24] and experiment [25] indicate that for this the ratio of gas gain to channel noise must then be greater than 25:1. For a readout with electronic noise of about

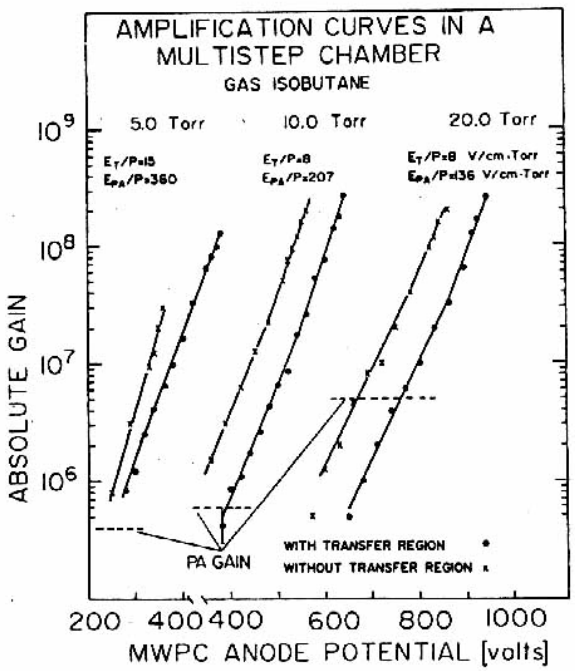

Fig. 2. Amplification curves for a MSC operated with isobutane at pressures of 5, 10 and 20 Torr. The absolute total gain of the MSCs is presented versus the anode potential of the MWPC, for constant values of the preamplification and transfer fields. The amplification factor of the first PPAC stage is represented by dashed lines.

Figure 15: Gas gains achieved in single-step and multistep avalanche chambers filled with low-pressure isobutane. From ref. [14]

2×10^3 electrons the gas gain must then be at least 10^5. This should be well within the stable region of operation of a single-gap chamber.

The expected chamber performance is summarized in Table 5.

Table 5: Resolution of the low-pressure TPC for 165-MeV/c muons, assuming its length is 45 cm. The device performance is essentially independent of whether methane, ethane or isobutane gas is used.

Parameter	Value
σ_P/P over 2 m	0.0015
$\sigma_x = \sigma_y$ (μm)	200
$\sigma'_x = \sigma'_y$ for 20 cm drift	0.001
σ_t (ns)	5

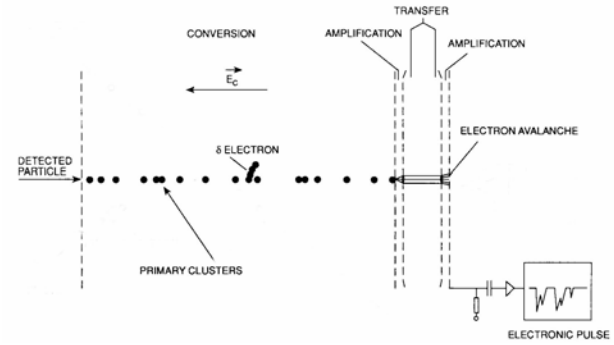

Figure 16: Electrode configuration for a multistep time projection chamber. From ref. [18]

4.7 Time Sampling

As noted in Table 4, the ionization electrons drift across the 45-cm-long chamber for 4.5-11 μsec. To this time must be added the desired livetime of the chamber, which depends on the filling characteristics of the RF cavities. These are expected to have a good fill for of order 5 μsec. Hence the total chamber live time is desired to be about 10 μsec. The beam cycle is expected to be 1-15 Hz.

To reconstruct the muon trajectories in space, the longitudinal position of each cluster must be reconstructed to about the same accuracy as its transverse coordinates, *i.e.*, to 200 μm. If we use methane as the chamber gas, then 200 μm corresponds to 2 ns of drift, according to Table 4. Thus the drift time of each cluster must be measured to about 2 ns.

This can be accomplished by recording the signal size in a sequence of time samples separated by several times the desired time resolution. An example of such a readout scheme is given in ref. [26]. For example, we could sample every 20 ns (50 MHz), or at 10 times the desired resolution. The signal:noise need only be about 10:1 to perform the time interpolation.

The average time separation between clusters in methane is 300 ns. There would be an average of 15 samples between clusters arriving from a trajectory exactly along the field lines, so confusion between adjacent cluster should be tolerably small. The total number of samples in the 10-μs detector live time is 500.

These parameters are well matched to the use of switched-capacitor arrays (SCA's) for analog-pipeline storage of the samples. Figure 17 sketches the concept of an SCA. Figure 18 shows a waveform transmitted through a 128-deep SCA, retaining 12-bit dynamic range. Figure 19 shows that SCA time sampling can be used to resolve pulse times to an accuracy better than 1% of the sampling interval.

The 512 16-channel SCA/ADC chip designed by S. Kleinfelder [27, 28] for the STAR TPC would be a good choice for the present experiment. Some R&D is needed to verify the performance of this SCA at 50 MHz, which is slightly beyond the range presently characterized [29]. The 16-channels of an SCA are multiplexed to a slow ($\approx$ 1 MHz) 12-bit ADC (on the SCA chip), permitting the 16×512 samples stored in each chip to be digitized in 8 msec between beam pulses. Each TPC would be instrumented with 80 16-channel preamps

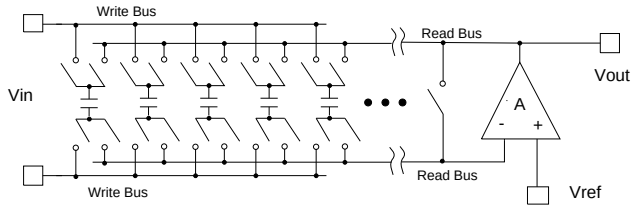

Figure 17: Sketch of the concept of a switched-capacitor array.

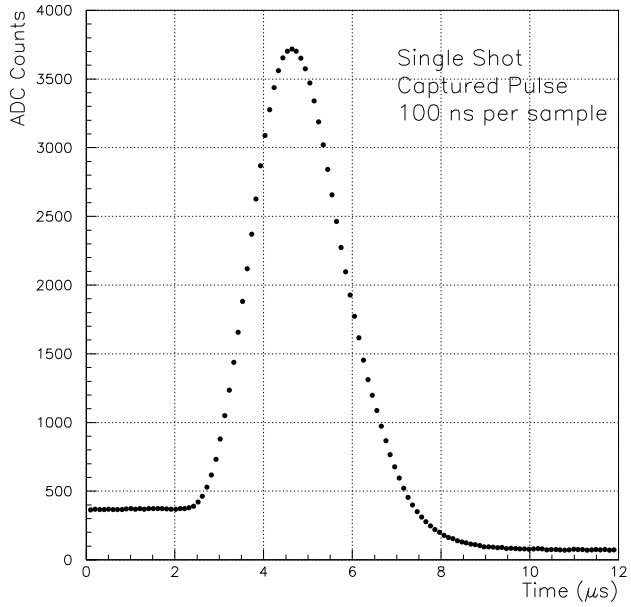

Figure 18: A waveform transmitted through a 128-deep SCA, retaining 12-bit dynamic range.

(for example, the STAR chip [30, 31] which can be set to a 100-ns shaping time via control voltages) and SCA chips that would be mounted at 1-cm intervals around the circumference of the cathode pad plane inside the detector pressure vessel. Each SCA/ADC chip dissipates only 0.1 Watt, and the STAR preamp chips dissipates 0.75 Watt; each TPC would dissipate about 75 Watt. The system cost of the STAR TPC readout electronics is about \$33/channel [29]

The Princeton group has built detector readouts based on 128-deep switched-capacitor arrays [32, 33].

An alternate sampling scheme could be based on use of one 25-MHz flash ADC for each of the 10,000 readout channels.

4.8 Rate Capability

Each TPC would have 1250 channels with 500 time samples each, for a total of some 600,000 x-y-t pixels. Each muon contributes about 20 clusters. Each cluster occupies about $3^3 = 27$ pixels, or about 500 pixels/track. Then 1200 muons would result in 100% occupancy. A safe

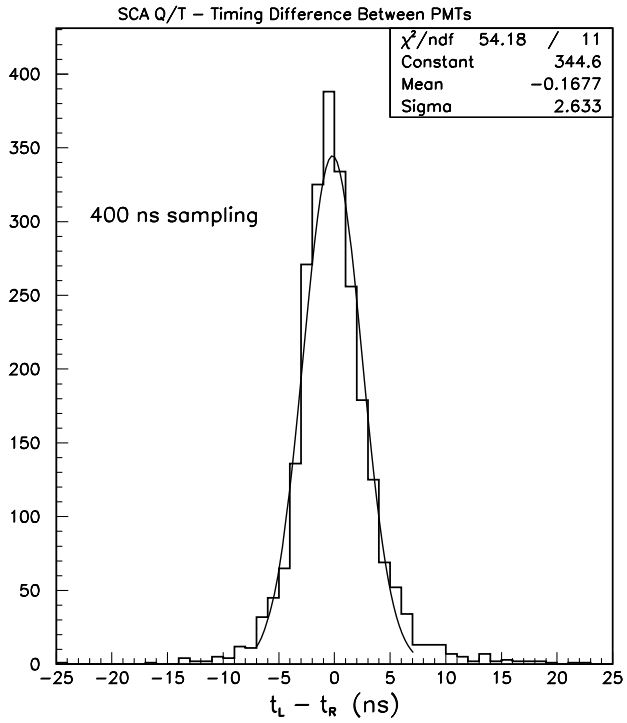

Figure 19: An SCA sampling at 400-ns intervals can resolve the pulse time to 3 ns.

operating regime would be about 10 muons per beam pulse.

The data rate would be about 5,000 samples/pulse, or 75,000 samples/sec at 15-Hz beam rate.

4.9 Diffusion

The preceding discussion has ignored the effect of diffusion on the detector resolution. This is a potentially serious problem in view of the long drift path in the proposed TPC. Furthermore, since the diffusion coefficient is proportional to the mean free path of the drifting electrons, diffusion is more pronounced at low pressures [34, 35]. [The Princeton group has demonstrated this effect in past detector studies [36].]

Our analysis must take into account the presence of the electric and magnetic fields. The case of $\mathbf{E} \parallel \mathbf{B}$ is, however, somewhat simpler to treat than $\mathbf{E} \perp \mathbf{B}$.

First, it is important to recall that a major goal of the tracking system is to measure velocity of the muon along beam axis, as needed to extrapolate the muon timing from the RF timing cavity to the entrance of the cooling apparatus. This leads to a demanding requirement on measurement of total momentum, and a weaker requirement on measurement of the track angle.

Recall also that measurement of total momentum in a bent-solenoid spectrometer is accomplished through measurement of the vertical offset of the guiding ray of the muon trajectory before and after the bent solenoid. For this measurement only transverse coordinates

of the muon trajectory are needed. Measurement of the track angle requires both transverse and longitudinal coordinates.

4.9.1 Transverse Diffusion

The solenoid field suppresses the transverse diffusion; the transverse mean free path is always less than twice the Larmor radius r_B, which is typically much less than the longitudinal mean free path. So despite the longer (longitudinal) mean free path at low pressure, transverse diffusion does not lead to difficulties for our measurements.

We begin more detailed discussion with consideration of the effect of pressure and electric field. Recall that the diffusion coefficient D is defined such that the rms spread σ of the electron's position (along some axis) after time t is

$$\sigma = \sqrt{2Dt} = \sqrt{\frac{2Dz}{v_d}}, \tag{81}$$

where the second form holds when the electron has a drift velocity v_d, and z is the drift distance.

The saturation drift velocity is $v_d \approx 10^7$ cm/s for methane, according to Fig. 14, which occurs for electric fields of about 1000 V/cm at STP. Then from Fig. 20 we deduce that the diffusion coefficient for methane is $D \approx 3000$ cm^{2}s^{-1} at STP.

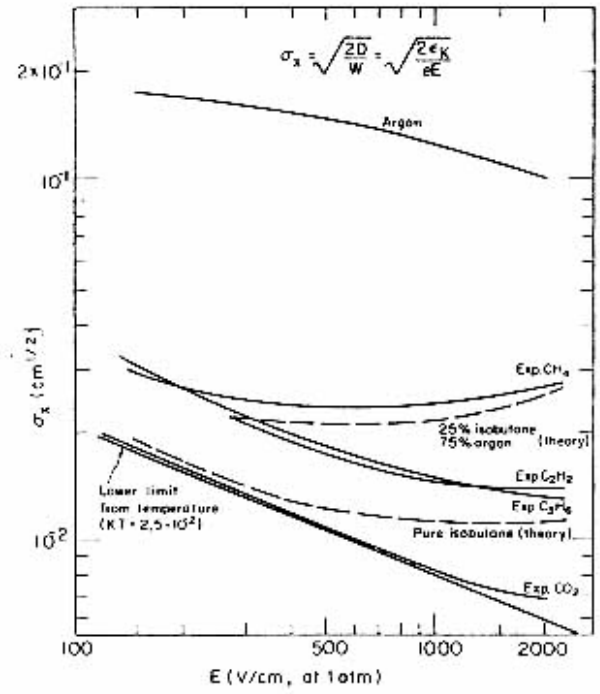

Figure 20: Diffusion over a 1 cm drift path for various gases. From [35].

We propose to adjust the pressure P, temperature T and electric field E to keep the drift velocity at saturation. Hence it is convenient to use a relation for the diffusion coefficient

given by Einstein (see. eq. 31.13 of [34]):

$$D \approx \frac{v_d kT}{eE}, \tag{82}$$

where k is Boltzmann's constant. With $kT \approx 1/40$ eV, eq. (82) predicts $D \approx 2500$ cm^{2}s^{-1} for methane at STP, in reasonable agreement with data.

Equation (82) then leads to the scaling law

$$D(E,T) = \frac{T}{T_0}\frac{E_0}{E} D(E_0, T_0). \tag{83}$$

For example, we are considering the merits of methane as a chamber gas, operating at $T \approx 100$K, and at pressure such that the drift velocity is saturated for $E = 10$ V/cm. Then from eq. (83) we infer that $D(100, 10) = 33D(300, 1000) = 10^5$ cm^{2}s^{-1}.

The scaled diffusion coefficient just deduced applies to the case of zero magnetic field, and to longitudinal diffusion when $\mathbf{E} \parallel \mathbf{B}$. In the latter case the transverse diffusion coefficient is reduced by a factor

$$\frac{r_B}{l} = \frac{v_d/\omega_B}{v_d\tau} = \frac{1}{\omega_B \tau}, \tag{84}$$

where r_B and ω_B are the Larmor radius and frequency of the electron in magnetic field B, l is the mean free path and τ is the mean time between collisions of the electron with gas molecules (see eq. 13.8 of [34]). The Larmor frequency is given by

$$\omega_B = 1.8 \times 10^{11} \text{ Hz} \times B \text{ [Tesla]}, \tag{85}$$

so $\omega_B \approx 5 \times 10^{11}$ Hz for $B = 3$ T. The collision time can be deduced from the basic relation for the drift velocity in terms of the electric field,

$$v_d \approx \frac{eE}{m}\tau, \tag{86}$$

so $\tau \approx 6 \times 10^{-9}$ s when $E = 10$ V/cm.

The transverse diffusion coefficient is therefore suppressed by a factor $1/\omega_B\tau \approx 1/3000$ compared to the longitudinal coefficient. That is, $D_\perp \approx 33$ cm^{2}s^{-1} at the proposed operating conditions. Even at the maximum drift distance of 45 cm, the uncertainty in transverse position due to diffusion is

$$\sigma_{\perp,\text{diffusion}}(45 \text{ cm}) \approx \sqrt{\frac{2 \cdot 33 \cdot 45}{10^7}} \text{ cm} = 170 \ \mu\text{m}. \tag{87}$$

That is, transverse diffusion for low-pressure, low-temperature methane leads to a position uncertainty that is less than our expected electronic resolution.

Note also that eqs. (82), (84) and (86) can be combined to yield

$$D_\perp \approx \frac{kT}{m\omega_B}, \tag{88}$$

for transverse diffusion in a magnetic field. The result is actually independent of pressure, and is smaller for low temperatures and high magnetic fields!

4.9.2 Longitudinal Diffusion

The longitudinal diffusion coefficient for electron drift at the saturation velocity $v_d = 10^7$ cm/s in methane at 100°K and 0.01 atmosphere was found from eqs. (82) and (83) and Fig. 20 to be $D_\parallel = 10^5$ cm^{2}s^{-1}. The resulting smearing of the location of an electron drifting along the (parallel) lines of fields **E** and **B** is

$$\sigma_z = \sqrt{\frac{2D_\parallel x}{v_d}} \equiv A\sqrt{z}, \tag{89}$$

where $A = 0.135$ cm$^{\frac{1}{2}}$. This is a significant uncertainty, and reduces the accuracy with which we could reconstruct the angle θ of the helical muon trajectory with respect to its guiding ray.

We estimate this uncertainty by supposing the tracking data is represented as a set of transverse coordinates u_i measured at longitudinal coordinates z_i. Coordinate u is measured on the surface of the helix and is orthogonal to z. Then we expect $u = z\tan\theta \approx z\theta$. We ignore the error in the measurement of u in comparison to that on the measurement of z. From the chi square

$$\chi^2 = \sum_i^N \frac{(z_i - u_i/\theta)^2}{\sigma_{z_i}^2} = \sum_i^N \frac{(z_i - u_i/\theta)^2}{A^2 z_i}, \tag{90}$$

we deduce that

$$\frac{1}{\sigma_\theta^2} = \frac{\partial\chi^2}{\partial\theta^2}, \qquad \text{and hence} \qquad \sigma_\theta = A\theta\sqrt{\frac{\theta}{Nz}}, \tag{91}$$

for N measurements at (roughly) uniform intervals over total length z. In the proposed configuration, $N = 15$, $z = 45$ cm, and the characteristic angle is $\theta_{\rm rms} = 0.05$ (Table 2). In this case we estimate

$$\sigma_{\theta,\rm diffusion} \approx 0.00006, \qquad \text{and} \qquad \frac{\sigma_{\theta,\rm diffusion}}{\theta} \approx 0.0012. \tag{92}$$

Thus despite sizable longitudinal diffusion, we should be able to measure track angles to the accuracy specified in Table 3, and also to the accuracy claimed in Table 5 for the TPC detector.

4.9.3 Diffusion When **E** $\perp$ **B**

Another possible configuration for the electrodes of the tracking chamber is such that the drift electric field **E** is transverse to the magnetic field **B**. As is well known, the drift path then includes a component in the direction of **E** $\times$ **B**. Of greater importance in the present case is the fact that the drift $\mathbf{v}_d$ velocity remains perpendicular to the magnetic field **B**, and so the component of the mean free path along the drift direction is reduced by a factor $r_B/l = 1/3000$, the ratio of the Larmor radius to the mean free path in zero magnetic field. In turn, the drift velocity is reduced by this factor and is now very slow: $v_d \approx 3 \times 10^3$ cm/s.

The transverse and longitudinal diffusion coefficients are the same as calculated for the case **E** $\parallel$ **B**. However, because the electrons drift for much longer times, the smearing due

to diffusion is much greater. Indeed, for a typical drift of $r = 10$ cm from the center of the chamber to the electrode at its outer radius,

$$\sigma_\perp = \sqrt{\frac{2D_\perp r}{v_d}} = \sqrt{\frac{2 \cdot 33 \cdot 10}{3 \times 10^3}} = 0.46 \text{ cm}, \qquad \sigma_\parallel = \sqrt{\frac{2D_\parallel r}{v_d}} = \sqrt{\frac{2 \cdot 10^5 \cdot 10}{3 \times 10^3}} = 26 \text{ cm}. \quad (93)$$

These large uncertainties apply to all electrons along a muon track, which is roughly parallel to **B**.

It appears that a configuration with $\mathbf{E} \perp \mathbf{B}$ is unsuitable for a low-pressure, long-drift-path detector.

4.10 Delta Rays

In general, when an atom of chamber gas is ionized by a high-energy charged particle, the ionization electron has sufficient energy to ionize additional atoms some distance away. Thus, each primary ionization leads to a cluster of ionization, also called a δ-ray, which can have large spatial extent in some cases. The spatial extent of the cluster is larger for lower-pressure gases. Does this effect compromise the chamber resolution?

Cluster measurements for hydrocarbon gases have been reported by Fischle *et al.* [37], with the approximate result that the average number of electrons per cluster is 1.5, with a probability distribution $P(n) \propto n^{-5/2}$, or equivalently, $P(n > n_0) = (2n_0)^{-3/2}$. Further, the average energy needed to create an ion pair is 30 eV. For example, clusters of more than 10 electrons occur about 1% of the time, corresponding to the primary ionization electron being produces with about 300 eV.

As for the case of diffusion, the strong magnetic field confines the motion of the ionization electrons to helices of very small radii, given by

$$r[\text{m}] = \frac{p[\text{MeV}/c]}{300B[\text{T}]} = \frac{\sqrt{\text{KE}[\text{MeV}]}}{300B[\text{T}]}. \quad (94)$$

For $B = 3$ T and KE = 100 eV, the helix radius is only 10 μm; even for KE = 10 keV, the radius is only 100 μm. Thus, δ-rays will have neglible effect on the transverse position resolution of the TPC.

It remains to characterize the effect of δ-rays on the longitudinal position resolution, where the spatial extent of the cluster is the same as in the absence of the the magnetic field. We estimate the spatial extent of a typical cluster of, say, 2 electron by three methods:

1. The cluster size is roughly equal to the mean free path of a 30-eV electron. This is also roughly equal to the mean free path of the drifting electrons. From information presented in sec. 4.9.1, we estimate this as $l = v_d\tau = 10^7 \times 6 \times 10^{-9} = 0.06$ cm = 600 μm for methane at 8.4 Torr.

2. If we suppose that the cross section σ for ionization of an atom is about 10^{-16} cm^2, then at 1/100 atmosphere at 20°C where the number density ρ is $N_A/22,400/100 \approx 2.7\times10^{17}$ atoms/cm^3, the mean free path for ionization is $l = 1/\rho\sigma \approx 1/27cm \approx 400$ μm.

3. A semi-empirical expression for the range of keV electrons in matter of molecular weight A, Z electrons/atom and mass density ρ g/cm^3 has been given by Feldman [38] as

$$\text{Range}[\mu\text{m}] \approx 0.025 \frac{A}{\rho Z^{p/2}} (\text{KE}[\text{MeV}])^p, \qquad \text{where} \quad p = \frac{1.2}{1 - 0.29 \log_{10} Z}. \tag{95}$$

For methane, $A = 16$, $Z = 10$, so the power is $p = 1.69$. At 1/100 atmosphere the mass density is 7.2×10^{-6} g/cm^3. Then, eq. (95) predicts a range of 8000 $(\text{KE}[\text{keV}])^{1.69}$ μm. For, say, KE = 100 eV, the predicted range is 160 μm.

Comparing the three estimates, we take 500 μm as the typical longitudinal cluster size for methane at 1/100 atmosphere. While large, this is still smaller than longitudinal diffusion for a drift of 1 cm, as found in sec. 4.9.2, and so will not be a problem.

A cluster of n electrons will have longitudinal extent of $(n-1)500$ μm, and rms size $1/\sqrt{12}$ times this: $\sigma_n \approx (n-1)144$ μm. For $n = 10$ this is similar to the longitudinal diffusion for the first cluster, whose drift distance is typically 1.5 cm. However, a cluster with $n = 10$ occurs only about 1% of the time, as noted above.

5 Auxiliary Timing Detector

In sec. 3.5 we noted that the RF timing technique is ambiguous for times too far off nominal. Hence we need an auxiliary timing device, capable of resolution the muon time to about 300 psec.

In fields of 1.5 Tesla of less, 100-150-psec timing is possible using Hamamatsu fine-mesh photomultipliers coupled to scintillator bars [39]. However, for fields above 1 Tesla the signal in the fine-mesh tubes drops precipitously. In contrast, the performance of microchannel-plate photomultipliers (MCP-PMT's) is hardly affected by a magnetic field aligned along the tube axis [40].

5.1 Fine-Mesh Photomultipliers Viewing Scintillator Bars

If the bent solenoid channel can operate at a field of 1.5 T or less the preferred option for the auxiliary timing detector will be Hamamatsu fine-mesh photomultipliers viewing scintillator bars. A candidate device is Hamamatsu model R5504 [41] whose outer diameter is 51 mm with a 36-mm diameter photocathode. The cost is about \$5k each.

Figure 21 shows how these PMT's might be arranged inside the solenoid channel to provide coverage over a radius of 10 cm.

Improved timing could be obtained by coupling the PMT's to quartz bars rather than scintillator, since the intrinsic time scale of the Čerenkov radiation process is femtoseconds compared to nanoseconds for scintillation. Indeed, time resolutions as good as $\sigma_t = 30$ ps have been reported in a recent study [42].

5.2 Microchannel-Plate PMT's Viewing Čerenkov Radiation

Should the auxiliary timing detector have to operate in a magnetic field above 1.5 Tesla, the principal option is microchannel-plate PMT's. These are more costly ($\approx$ \$10k each) and

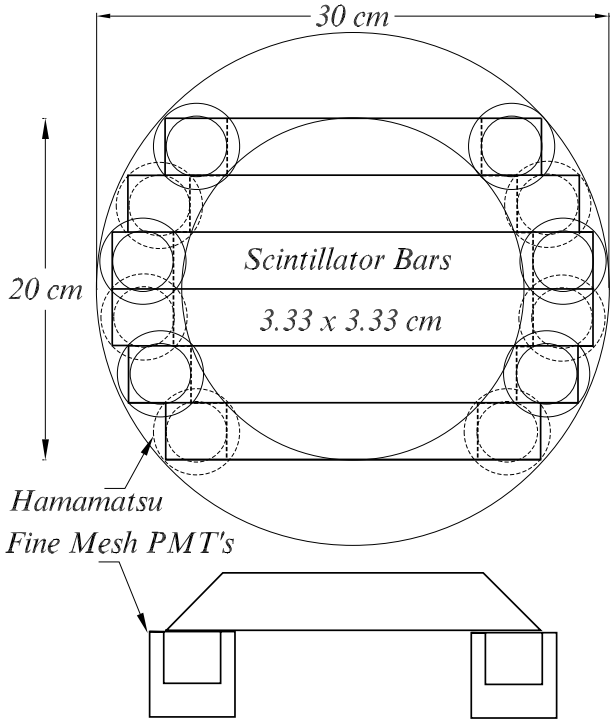

Figure 21: Sketch of a possible arrangement of 12 Hamamatsu R5504 fine-mesh PMT's viewing six 3.33×3.33 cm^2 scintillator bars entirely within the 30-cm-diameter, 1.5-T solenoid channel. Six PMT's face upstream and six face downstream.

have smaller photocathodes (11-mm diameter) than fine-mesh PMT's.

The timing capability of an MCP-PMT is, however, superior. Figure 22 shows the transit-time spectrum for a Hamamatsu R3809 and an R2809 MCP-PMT [43]. From the data shown, the R3809 device is capable of time resolution of $\sigma_t = 12$ ps for single photoelectrons, if the signal is not degraded by associated pulse-shaping electronics. For a signal of n photoelectrons, the time resolution might improve by a factor of $1/\sqrt{n}$ under favorable circumstances.

5.2.1 Bench Test of MCP-PMT Timing

We have tested the timing capability of two R3809 MCP-PMT's in the configuration shown in Fig. 23 [44]. A Sr^{90} β source impinges on a 3-mm-thick quartz plate. A portion of the β spectrum has momentum such that the Čerenkov angle is 45° after the light emerges from the quartz plate. The two R3809 MCP-PMT's were placed 90° apart, and the time difference measured between the first Čerenkov photon in each device. The results are shown in Fig. 24, and indicates $\sigma_t = 55/\sqrt{2} = 39$ ps for each device in this test. The signal in each detector was due to a single photoelectron in most cases.

While we speculate that this result is larger than that claimed by Hamamatsu due to jitter in the discriminator we used, this has not been studied further to date.

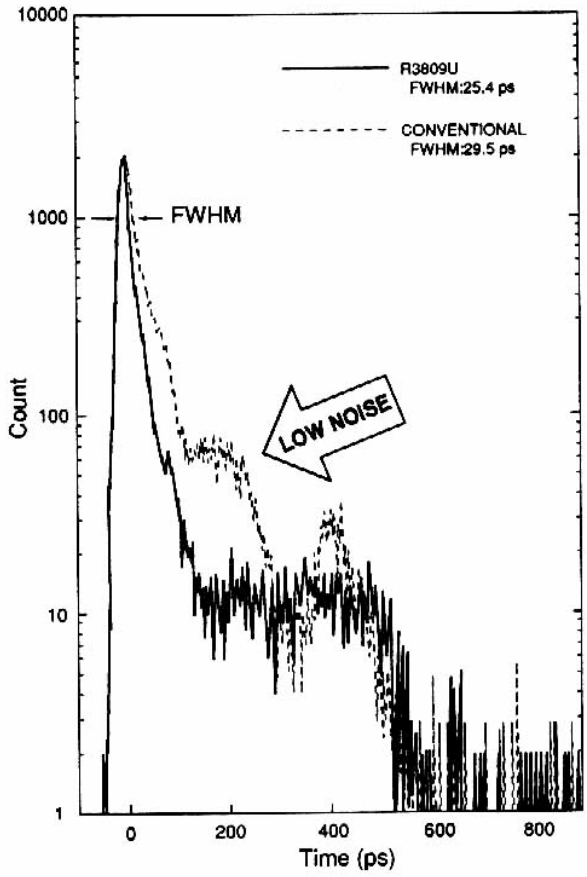

Figure 22: Spectrum of transit-time jitter in a Hamamatsu R3809 MCP-PMT.

5.2.2 MCP-PMT Configuration for the Cooling Experiment

Quartz has an index of refraction of $n \approx 1.47$ for visible light, and so the minimum angle of incidence for internal reflection is 43°. Muons of 165 MeV/c have $\beta = 0.84$ and the corresponding Čerenkov angle is 36°. Hence, no Čerenkov light is internally reflected for 165-MeV/c muons at normal incidence to a quartz bar.

The muons must have angle of incidence at least 7° for any Čerenkov light to be internally reflected. The optimal angle of incidence is 54°, in which case one ray of the Čerenkov cone points directly down the bar.

Figure 25 illustrates a configuration in which the average angle of incidence would be 45°. To minimize the path length, the quartz bars are arranged in two arrays at ±45° to the muon beam. The bars are read out only at the end in the direction of the forward Čerenkov light.

The active area of the photocathode of R3809U MCP-PMT's is only 11 mm in diameter, so each tube is matched to a quartz bar of 1×1 cm^2 cross section. Since the diameter of the MCP-PMT's is considerably larger than 1 cm, most bars must have an angled light guide to bring the light to locations where different tubes don't interfere with one another. Figure 25 shows how this might be accomplished if the R3809U devices could be repackaged into a 3

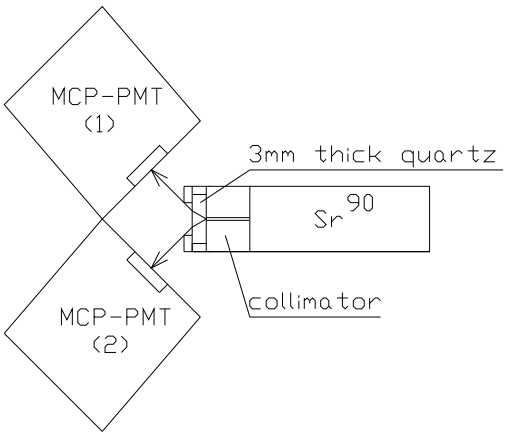

Figure 23: Layout of the timing test of two R3809 MCP-PMT's.

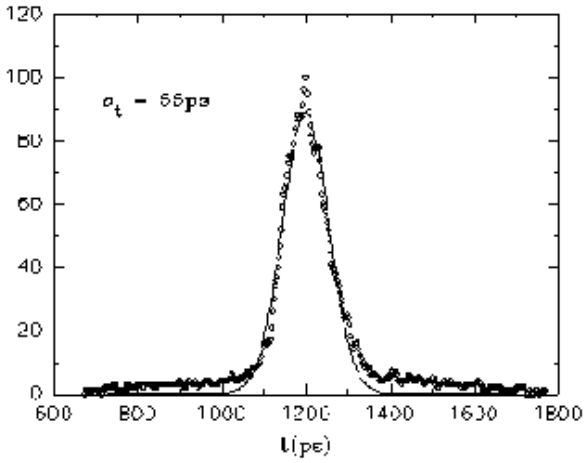

Figure 24: Distribution of time differences between Čerenkov light received by two R3809 MCP-PMT's.

cm diameter; since the basic structure of the MCP-PMT is 2.5 cm in diameter this may be possible.

A key question is whether such a detector could produce time resolution better than the single-photoelectron transit-time jitter, which is 12 ps (σ) for the R3809U MCP-PMT's.

To answer this, simulation of timing performance of such an array has been made with an EXCEL spreadsheet developed by Mats Selen in association with ref. [42]. This simulation includes the effects of dispersion and phototube quantum efficiency, and is well validated by data [42].

Some preliminary conclusions are reported here; extensive updates will follow shortly.

We use the simulation to calculate the time of arrival of each Čerenkov photon at the face of the PMT, and record only those photons that produce photoelectrons according to a cut based on the PMT quantum-efficiency spectrum. For example, the rms spread in arrival

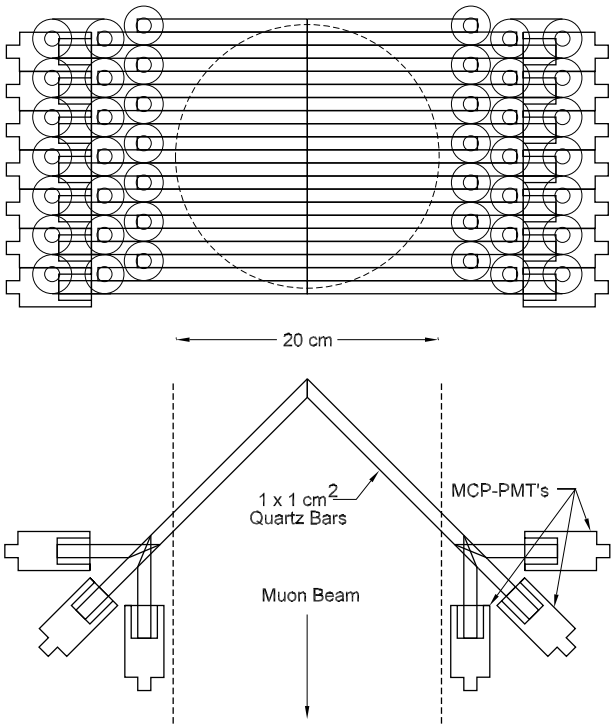

Figure 25: Layout of an auxiliary timing device based on Hamamatsu R3809 MCP-PMT's viewing Čerenkov light from 1×1 cm^2 quartz bars.

times of the earliest Čerenkov photoelectron is 11 ps from a 165-MeV/c muon incident on a 1×1 cm^2 bar at 45° and 25 cm from the PMT.

As a simple model of the effect of the PMT on the timing, we smear the arrival time of each photon by the transit-time jitter of the PMT, 12 ps for the R3809U MCP-PMT's and 160 ps for the fine-mesh PMT's. Then, the rms spread in arrivel times of the earliest photoelectron in the example above is 15 ps. This is slightly less than the result of combining 11 and 12 ps in quadrature, which indicates that occasionally the second created photoelectron fluctuates to become the first detected one.

This result also indicates that a timing algorithm based on the first detected photoelectron would not yield resolution better than 15 ps for the device sketched in Fig. 25. Can we do better by using information from more than one photoelectron?

Kichimi *et al.* [42] reported time resolution of 30 ps for distances up to 30 cm from a Hamamatsu H2431 fine-mesh PMT (4.6-cm active diameter) coupled to a 2×4 cm^2 quartz bar, when a 1-GeV pion entered the bar at 40° angle of incidence. The transit-time jitter for these PMT's is stated as 160 ps by Hamamatsu. We can reproduce this behavior in our simulation supposing the transit-time jitter is actaully 120(?) ps , and that the timing algorithm is based on the arrival time of the 10th photoelectron.

This desirable behavior can occur because typically 10 (?) photoelectrons arrive within the transit-time jitter of the fine-mesh PMT's. However, the transit-time jitter of the MCP-PMT's is so short that typically only a single photoelectron arrives during this interval, and

the arrival times of the photoelectrons are essentially decoupled. Thus, the best time resolution obtainable with the MCP-PMT's is based on the time of the first detected photoelectron, and is $\sigma = 15$ ps.

Hence, the MCP-PMT detector would not provide the 6-ps time resolution needed to located the muons with respect to the cooling rf cycle (recall sec. 2.4). However, such a device would be excellent as an auxiliary timing device.

5.3 e-μ-π Identification by Time of Flight

Either the fine-mesh PMT's or the MCP-PMT's can provide timing accurate enough to resolve the ambiguity in the RF timing cavity. They can also provide a good measure of the muon's time of flight over the 3-meter path between the auxiliary timing detector and the RF timing cavity. This should permit identification of electrons, muons and pions.

Indeed, the time-of-flight difference per meter between particles of masses m_1 and m_2 at momentum P is

$$\Delta t = \frac{1}{\beta_1 c} - \frac{1}{\beta_2 c} = \frac{\sqrt{1+(m_1 c/P)^2} - \sqrt{1+(m_2 c/P)^2}}{c}. \tag{96}$$

At 165-MeV/c momentum electrons arrive earlier than muons by 0.625 ns/m and pions arrive later by 0.407 ns/m.

A potential problem with the proposed scheme is the ambiguity in the timing measurement of the RF timing cavity, whose period is 1.25 ns. We will select particles whose time is within ± 120 ps of the start of an RF cycle. But the RF measurement alone is ambiguous as to which half cycle the particle is in, *i.e.*, ambiguous to multiples of 0.625 ns. Thus the time-of-flight technique will work best if both the e-μ and the μ-π time differences of odd multiples of 312.5 ps.

This criterion cannot be met exactly. The best choice of flight path in the range 3-4 m is 3.63 m, for which both the e-μ and the μ-π time differences differ from multiples of 0.625 ns by 230 ps. If the timing resolution of the auxiliary timing device is 100 ps we would have only 2.3-σ separation between μ's and e's or π's.

e-μ separation would be maximized at (effectively) 312 ps for a flight path of 3.5 m, at which the μ-π separation is only (effectively) 177 ps. μ-π separation would be maximized at (effectively) 312 ps for a flight path of 3.82 m, at which the e-μ separation is only (effectively) 105 ps.

Clearly the particle identification would benefit from an auxiliary timing device with resolution of 30 ps rather than 100 ps. This accuracy could be achieved with either fine-mesh PMT's or MCP-PMT's in a configuration such as that of Fig. 25.

References

[1] Many of the unpublished papers cited below can be found at
http://physics.princeton.edu/~mcdonald/mumu

[2] D.R. Nicholson, *Introduction to Plasma Theory* (Wiley, 1983), secs. 2.3-4.

[3] M.A. Green, R. Byrnes and S.J. St. Lorant, *Estimating the Cost of Superconducting Magnets and The Refrigerators Needed to Keep Them Cold*, LBL-30824 (June 1991), http://physics.princeton.edu/~mcdonald/examples/magnets/green_lbl-30824.pdf

[4] K.L. Brown *et al.*, *TRANSPORT* manual, SLAC-91, Rev. 2 (May 1977), p. 115, http://physics.princeton.edu/~mcdonald/examples/accel/brown_slac-91-rev2.pdf

[5] H. Wiedemann, *Particle Accelerator Physics II*, (Springer, 1995), sec. 3.3.3.

[6] K.T. McDonald and D.P. Russell, *Methods of Emittance Measurement*, in *Frontiers of Particle Beams; Observation, Diagnosis and Correction*, M. Month and S. Turner, eds. (Springer, 1989), p. 122, physics.princeton.edu/~mcdonald/atf/emit_meas.pdf

[7] J. Haimson, *Microwave and Beam Optics Design of Standing Wave Transverse Magnetic Deflection Systems*, Varian Technical Associates Memorandum TMO-90 (February 1966).

[8] K.T. McDonald and E.J. Prebys, *Bunch-Timing Measurement in the Muon Cooling Experiment Via Rectangular $TE_{0,1,n}$ RF Cavities*, Princeton/$\mu\mu$/97-5 (July 18, 1997), http://physics.princeton.edu/~mcdonald/mumu/timing_071397.pdf

[9] K.T. McDonald and E.J. Prebys, *Bunch-Timing Measurement in the Muon Cooling Experiment Via a Rectangular $TM_{2,1,0}$ RF Cavity*, Princeton/$\mu\mu$/97-6 (July 18, 1997), http://physics.princeton.edu/~mcdonald/mumu/deflection.pdf

[10] K.T. McDonald and E.J. Prebys, *Bunch-Timing Measurement in the Muon Cooling Experiment Via a Square $TM_{1,1,0}$ or a Cylindrical $TM_{0,1,0}$ RF Accelerating Cavity*, Princeton/$\mu\mu$/97-7 (July 24, 1997), http://physics.princeton.edu/~mcdonald/mumu/timing_072497.pdf

[11] F. Binon *et al.*, *Low Pressure Multiwire Proportional Chambers with High Time Resolution for Strongly Ionizing Particles*, Nucl. Instr. and Meth. **94**, 27 (1971), http://physics.princeton.edu/~mcdonald/examples/detectors/binon_nim_94_27_71.pdf

[12] A. Breskin, *A Subnanosecond Low Pressure MWPC for Heavily Ionizing Particles*, Nucl. Instr. and Meth. **141**, 505 (1977), http://physics.princeton.edu/~mcdonald/examples/detectors/breskin_nim_141_505_77.pdf

[13] A. Breskin *et al.*, *Heavy Ion Timing with Very Low Pressure MWPC's*, Nucl. Instr. and Meth. **165**, 125 (1979), http://physics.princeton.edu/~mcdonald/examples/detectors/breskin_nim_165_125_79.pdf

[14] A. Breskin, *Progress in Low-Pressure Gaseous Detectors*, Nucl. Instr. and Meth. **196**, 11 (1982), http://physics.princeton.edu/~mcdonald/examples/detectors/breskin_nim_196_11_82.pdf

[15] A. Breskin *et al.*, *Heavy Particle Timing and Imaging with Low-Pressure MWPC's*, Nucl. Instr. and Meth. **217**, 107 (1983), http://physics.princeton.edu/~mcdonald/examples/detectors/breskin_nim_217_107_83.pdf

[16] A. Breskin, G. Charpak and S. Majewski, *On the Low-Pressure Operation of Multistep Avalanche Chambers*, Nucl. Instr. and Meth. **220**, 349 (1984), http://physics.princeton.edu/~mcdonald/examples/detectors/breskin_nim_220_349_84.pdf

[17] A. Breskin and R. Chechik, *High Accuracy Imaging of Single Photoelectrons by Low-Pressure Multistep Avalanche Chamber Coupled to a Solid Photocathode*, Nucl. Instr. and Meth. **227**, 24 (1984), http://physics.princeton.edu/~mcdonald/examples/detectors/breskin_nim_227_24_84.pdf

[18] A. Pansky *et al.*, *Applications of Gaseous Electron Counting Detectors*, Nucl. Instr. and Meth. A **323**, 294 (1992), http://physics.princeton.edu/~mcdonald/examples/detectors/pansky_nim_a323_294_92.pdf

[19] D.F. Anderson, *A Photoionization Detector for the Detection of Xenon Light*, IEEE Trans. Nuc. Sci. **28**, 842 (1981), http://physics.princeton.edu/~mcdonald/examples/detectors/anderson_ieeetns_28_842_81.pdf

[20] D.F. Anderson, *Extraction of Electrons from a Liquid Photocathode into a Low-Pressure Wire Chamber*, Phys. Lett. B **118**, 230 (1982), http://physics.princeton.edu/~mcdonald/examples/detectors/anderson_pl_118b_230_82.pdf

[21] C. Lu, K.T. McDonald and Y. Zhu, *Helium Gas Mixtures for Ring Imaging Čerenkov Detectors with CsI Photocathodes*, Nucl. Instr. and Meth. A **334**, 328 (1993), http://physics.princeton.edu/~mcdonald/examples/detectors/lu_nim_a334_328_93.pdf

[22] J. Va'vra, *Wire Chamber Gases*, Nucl. Instr. and Meth. A **323**, 34 (1992), http://physics.princeton.edu/~mcdonald/examples/detectors/vavra_nim_a323_34_92.pdf

[23] I. Lehraus, R. Matthewson and W. Tejessy, *dE/dx Measurements in Ne, Ar, Kr, Xe and Pure Hydrocarbons*, Nucl. Instr. and Meth. **200**, 199 (1982), http://physics.princeton.edu/~mcdonald/examples/detectors/lehraus_nim_200_199_82.pdf

[24] E.J. Prebys, *Proposal for a Wire-Chamber-Based CsI Photocathode for a B-Factory RICH*, Princeton/HEP/94-19 (Jan. 19, 1994), http://physics.princeton.edu/~mcdonald/examples/detectors/prebys_princeton-hep-94-19.pdf

[25] C. Lu *et al.*, *Characterization of CsI Photocathodes for Use in a Fast RICH Detector*, Nucl. Instr. and Meth. A **366**, 60 (1995), http://physics.princeton.edu/~mcdonald/examples/detectors/lu_nim_a366_60_95.pdf

[26] D. Goldner, R. Horisberger and H. Kolanoski, *Study of Time and Charge Resolution of Drift Chamber Pulses Using a Fast VLSI Waveform Sample Chip*, PSI-PR-95-10 (June 1995), http://physics.princeton.edu/~mcdonald/examples/detectors/goldner_psi-pr-95-10.pdf

[27] S.R. Klein *et al.*, *Front End Electronics for the STAR TPC*, IEEE Trans. Nuc. Sci. **43**, 1768 (1996), http://physics.princeton.edu/~mcdonald/examples/detectors/klein_ieeetns_43_1768_96.pdf

[28] P. Barale, *STAR SCA/ADC Datasheet*, http://physics.princeton.edu/~mcdonald/examples/detectors/barale_star_sca-adc.pdf

[29] Spencer Klein, private communication.

[30] E. Beuville *et al.*, *A Low Noise Amplifier-Shaper with Tail Correction for the STAR Detector*, IEEE Trans. Nuc. Sci. **43**, 1619 (1996), http://physics.princeton.edu/~mcdonald/examples/detectors/beuville_ieeetns_43_1619_66.pdf

[31] T. Noggle, *SAS Specification: Integrated 16 Channel Preamp/Shaper*, (Sept. 26, 1994).

[32] R.L. Wixted *et al.*, *A 32-Channel Waveform Sampling FASTbus Module with Local DSP Processing*, Nucl. Instr. and Meth. A **386**, 483 (1997), http://physics.princeton.edu/~mcdonald/examples/detectors/wixted_nim_a386_483_97.pdf

[33] T. Liu *et al.*, *A Switched Capacitor Based Charge-to-Time Convertor*, Princeton/HEP/96-5 (May 19, 1996), http://physics.princeton.edu/~mcdonald/examples/detectors/liu_princeton-hep-96-05.pdf

[34] W.P. Allis, *Motions of Ions and Electrons*, *Handbuch der Physik*, **21**, 383 (Springer, 1956), http://physics.princeton.edu/~mcdonald/examples/detectors/allis_hdp_21_383_56.pdf

[35] V. Palladino and B. Sadoulet, *Application of the Classical Theory of Electrons in Gases to Drift Proportional Chambers*, Nucl. Instr. and Meth. **128**, 323 (1975), http://physics.princeton.edu/~mcdonald/examples/detectors/palladino_nim_128_323_75.pdf

[36] W.S. Anderson *et al.*, *Investigations of Single-Electron Avalanches in a Proportional Drift Tube*, in *Symposium on Detector Research and Development for the Superconducting Super Collider*, T. Dombeck *et al.*, eds. (World Scientific, 1991), physics.princeton.edu/~mcdonald/papers/anderson_ssc_ftworth_222_90.pdf

[37] H. Fischle *et al.*, *Experimental determination of ionization cluster size distributions in counting gases*, Nucl. Instr. and Meth. A **301**, 202 (1991), http://physics.princeton.edu/~mcdonald/examples/detectors/fischle_nim_a301_202_91.pdf

[38] C. Feldman, *Range of 1-10 KeV Electrons in Solids*, Phys. Rev. **117**, 455 (1960), http://physics.princeton.edu/~mcdonald/examples/detectors/feldman_pr_117_455_60.pdf

[39] V. Sum *et al.*, *A Time-of-Flight Array for 1 to 2 GeV/c Particles*, Nucl. Instr. and Meth. A **326**, 489 (1993), http://physics.princeton.edu/~mcdonald/examples/detectors/sum_nim_a326_489_93.pdf

[40] H. Kichimi *et al.*, *Timing Characteristics of Micro-Channel Plate and Fine Mesh Photomultipliers Tubes in a 1 T Field*, Nucl. Instr. and Meth. A **325**, 451 (1993), http://physics.princeton.edu/~mcdonald/examples/detectors/kichimi_nim_a325_451_93.pdf

[41] Technical Data Sheet, *Fine Mesh PMT Series for High Magnetic Field Environments*, Hamamatsu Photonics (Oct. 1994), http://physics.princeton.edu/~mcdonald/examples/detectors/hamamatsu_pmt_fine_mesh.pdf

[42] H. Kichimi *et al.*, *The Čerenkov correlated timing detector: beam test results from quartz and acrylic bars*, Nucl. Instr. and Meth. A **371**, 91 (1996), http://physics.princeton.edu/~mcdonald/examples/detectors/kichimi_nim_a371_91_96.pdf

[43] R3809U Technical Data Sheet, Hamamatsu Photonics (Aug. 1992), http://physics.princeton.edu/~mcdonald/examples/detectors/hamamatsu_R3809U-50.pdf

[44] C. Lu, D.R. Marlow and K.T. McDonald, *First Tests of the Timing Resolution of Microchannel-Plate Photomultipliers Viewing Čerenkov Radiation*, Princeton/HEP/94-11 (June 18, 1994), physics.princeton.edu/~mcdonald/mumu/mcptest.pdf